Modeling Iron and Light Controls on the Summer *Phaeocystis antarctica* Bloom in the Amundsen Sea Polynya

Hilde Oliver[1] iD, Pierre St-Laurent[2] iD, Robert M. Sherrell[3,4] iD, and Patricia L. Yager[1] iD

[1]University of Georgia, Department of Marine Sciences, University of Georgia, Athens, GA, USA, [2]Center for Coastal Physical Oceanography, Old Dominion University, Norfolk, VA, USA, [3]Department of Marine and Coastal Sciences, Rutgers University, New Brunswick, NJ, USA, [4]Department of Earth and Planetary Sciences, Rutgers University, Piscataway, NJ, USA

Abstract Of all the Antarctic coastal polynyas, the Amundsen Sea Polynya is the most productive per unit area. Observations from the 2010–2011 Amundsen Sea Polynya International Research Expedition (ASPIRE) revealed that both light and iron can limit the growth of phytoplankton (*Phaeocystis antarctica*), but how these controls manifest over the bloom season is poorly understood, especially with respect to their climate sensitivity. Using a 1-D biogeochemical model, we examine the influence of light and iron limitation on the phytoplankton bloom and vertical carbon flux at 12 stations representing different bloom stages within the polynya. Model parameters are determined by Bayesian optimization and assimilation of ASPIRE observations. The model-data fit is most sensitive to phytoplankton physiological parameters, which among all model parameters are best constrained by the optimization. We find that the 1-D model captures the basic elements of the bloom observed during ASPIRE, despite some discrepancies between modeled and observed dissolved iron distributions. With this model, we explore the way iron availability, in combination with light availability, controlled the rise, peak, and decline of the bloom at the 12 stations. Modeled light limitation by self-shading is very strong, but iron is drawn down as the bloom rises, becoming limiting in combination with light as the bloom declines. These model results mechanistically confirm the importance of climate-sensitive controls like stratification and meltwater on phytoplankton bloom development and carbon export in this region.

1. Introduction

Coastal polynyas, areas of seasonally open waters surrounded by sea ice, account for 65% of all Antarctic continental shelf primary production (Arrigo & Van Dijken, 2003). The Amundsen Sea Polynya (ASP) supports rates of net primary production as high as 2.5 gC m^{-2} day^{-1} (Arrigo et al., 2012; Arrigo & Van Dijken, 2003), 3–5 times greater than peak rates observed in the marginal ice zone (Arrigo et al., 2012, 2008) and the greatest of all Antarctic polynyas (Arrigo & Van Dijken, 2003). *Phaeocystis antarctica*, a colony-forming prymnesiophyte, dominates the blooms of the ASP (Ducklow et al., 2015; Kim et al., 2015, 2016; Lee, Park, et al., 2016; Lee, Yang, et al., 2016; Yager et al., 2016). This bloom is important to understanding the role of Antarctic polynyas in the global carbon cycle (Kim et al., 2016; Lee et al., 2017; Yager et al., 2016), but climate-sensitive factors of the bloom are not well understood.

Both light and the micronutrient iron (Fe) are important controls on the productivity in the polynya (Alderkamp et al., 2015; Schofield et al., 2015). Springtime sea ice retreat (1) frees the water column from shading by sea ice (Arrigo et al., 2012; Hahm et al., 2014) and (2) enhances stratification with the introduction of buoyant sea ice melt and solar warming, rendering the polynya favorable to phytoplankton growth. The very high chlorophyll *a* (Chl *a*) concentrations (up to 20 mg/m^3; Yager et al., 2016) result in shallow euphotic depths because of phytoplankton self-shading, however. Thus, light can limit productivity during the summer, and phytoplankton growth depends on the depth of the upper mixed layer and the vertical mixing rate (Park et al., 2017; Schofield et al., 2015).

The unusually high productivity of the ASP has also been attributed to a large supply of bioavailable Fe (Arrigo et al., 2015; Sherrell et al., 2015; Yager et al., 2012). This flux of iron to the euphotic zone is derived in part from buoyancy-driven upwelling caused by nearby melting glaciers (Gerringa et al., 2012; Greisman, 1979; St-Laurent et al., 2017) and also results from Circumpolar Deep Water contributions and seafloor
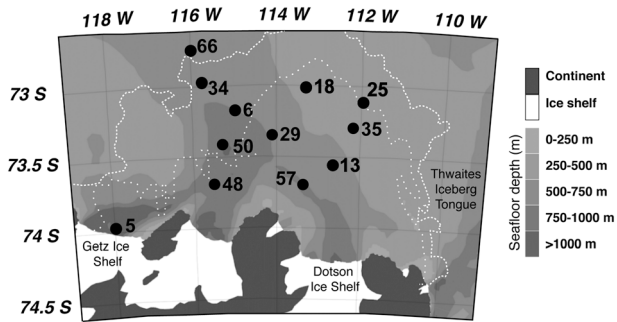
Figure 1. Geographic map of the Amundsen Sea Polynya (from Yager et al., 2016) and the 12 stations where the 1-D model is applied. The white lines indicate the edge of the open water (Mu et al., 2014) on 19 November 2010 (dotted) and 2 January 2011 (dashed), showing how the northern stations experienced fewer ice-free days.

sedimentary inputs (St-Laurent et al., 2017). The importance of dissolved Fe (dFe) to the bloom is supported by measurements of depleted trace metals in the ASP, with surface dFe drawn down to concentrations that limit phytoplankton growth (Alderkamp et al., 2015; Sherrell et al., 2015), whereas inorganic macronutrients are not reduced to limiting concentrations (Lee et al., 2012; Yager et al., 2016). Shipboard incubation experiments also indicate some iron stress during the growth phase of the bloom (Alderkamp et al., 2015). Additions of dFe to both high- and low-light incubations resulted in higher maximum Chl a normalized photosynthesis rates (P^*_{max}), suggesting iron limitation effects on the primary productivity of the phytoplankton. Both lateral advective processes and vertical mixing play a role in delivery of dFe to the upper water column (St-Laurent et al., 2017, 2019). ASP biogeochemical processes have been successfully accounted for in a 1-D framework, however. A well-balanced carbon budgeting exercise assuming no horizontal inputs can account for the bloom in the ASP (Yager et al., 2016), although uncertainty in the results was attributed in part to the assumption of one dimensionality as well as temporal variability. Modeling the ASP upper ocean with a 1-D model helps assess the roles of biological cycling and scavenging on distributions of dFe, as well as to test the extent to which the bloom can be resolved without accounting for lateral transport processes.

Light and nutrient supply in the ASP are likely to be altered rapidly with global climate change. While predicted shortening of sea ice duration (Stammerjohn et al., 2008, 2015) allows light availability for phytoplankton growth over a larger area, prolonged open water duration combined with stronger wind mixing may result in deeper mixed layers and thus increased light limitation (Park et al., 2017). In addition, increased fluxes of glacial meltwater to the ASP may increase the flux of dFe to the polynya, relieving iron limitation. Understanding the mechanisms controlling the full seasonal bloom will enable better projections of the future of the ASP ecosystem under anthropogenic climate change.

This study seeks to address the question of the relative importance of light versus iron limitation for the progression of the *P. antarctica* bloom in the ASP. We use a 1-D physical model coupled to a nitrogen and iron biogeochemical model to simulate the bloom at 12 Amundsen Sea Polynya International Research Expedition (ASPIRE) stations where the bloom was observed in austral summer 2010–2011 (Yager et al., 2016, 2012; Figure 1). In addition to isolating controls on the bloom, we also test the sensitivity of the results to key parameters of the biogeochemical model, which is used within a high-resolution, 3-D ocean circulation model (St-Laurent et al., 2017, 2019).

2. Methods

2.1. Overview

We developed a 1-D, nitrate-, light-, and iron-limited Nitrogen-Phytoplankton-Zooplankton-Detritus (NPZD) ecosystem model by adapting the iron-limited NPZD model developed by Fiechter et al. (2009) to the coastal environment in the Southern Ocean. Our iron-nitrate NPZD model is embedded within a vertical mixing model that is a part of the Regional Ocean Modeling System (ROMS). While lateral transport processes are important in the ASP (St-Laurent et al., 2017, 2019), the 1-D model is run with the assumption that the biogeochemical properties of the Winter Water "reserve" are sufficient to reproduce the bloom in the ASP, an assumption that has proven to be reasonably robust by a 1-D carbon budgeting effort (Yager et al., 2016). Taking advantage of the low computational cost of the 1-D model, we test its sensitivity to variations in the biogeochemical parameters, as well as the extent to which ASPIRE observations can be reproduced without the influence of lateral transport over the course of the bloom.

2.2. ROMS 1-D Model

We use the 1-D ROMS/biogeochemical model at 12 ASPIRE bloom stations (Figure 1) from 1 October 2010 to 31 March 2011 (6 months). These stations are the same as those considered by Yager et al. (2016), except for Station 68, a sea ice-covered station on the shelf break that we did not include since it was far from the
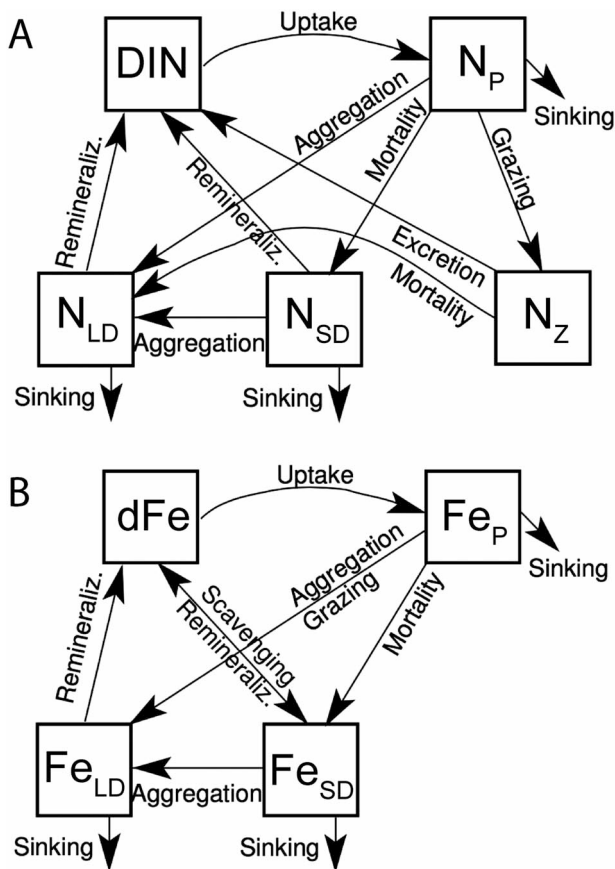
Figure 2. State variables and fluxes in the biogeochemical model: (a) nitrogen cycle and (b) iron cycle. Note that zooplankton-associated iron is not explicitly represented in the iron budget. Grazing is instead represented as a flux from phytoplankton (Fe_P) to large detritus (Fe_{LD}) Fe pools. Subscripts: P = phytoplankton-associated; SD = small detritus; LD = large detritus; DIN = dissolved inorganic nitrogen.

polynya. The observations from these stations span from 14 December 2010 to 5 January 2011, representing the beginning and rise of the bloom. The 1-D model uses a 9-min time step and represents the upper 210 m of the water column with 30 vertical levels. The model vertical resolution is highest in the surface layer (2- to 4-m resolution in the top 25 m) and lowest in the bottom layer (maximum of 15.5-m resolution at 210 m). The model physics evolve over time according to vertical mixing (Large et al., 1994) and surface forcing. The model physics are not affected by biogeochemical cycling in the model, however. The prognostic variables of the physical component of the model are temperature, salinity, horizontal velocity, and sea surface height (for a detailed description see Shchepetkin & McWilliams, 2005; Hedström, 2009).

2.3. The Iron-Nitrate NPZD Model

The biogeochemical model used in this study is a modified version of the iron-, light- and nitrate-limited NPZD model developed by Fiechter et al. (2009) for ROMS in the Gulf of Alaska. Phytoplankton growth is determined by a maximum specific rate and a multiplicative function of iron, nitrate, and light availability relative to saturating values. The model considers the cycles of both nitrogen and iron (Figure 2), allowing for explicit iron and nitrate limitation on the rate of nutrient uptake using Michaelis-Menten kinetics. The state variables of the nitrogen and iron cycles assumed in this study are similar to those in the original Fiechter et al. (2009) model. Since nitrate is the dominant form of dissolved inorganic nitrogen (DIN) in the ASP (Yager et al., 2016), nitrate is the sole nutrient in the model's nitrogen cycle, and we use nitrate and DIN interchangeably throughout this study. All source and sink terms are calculated at every model depth and at each time step in ROMS.

We modify the Fiechter et al. (2009) model by (1) adding a second size-specific detrital pool, (2) aggregating of phytoplankton and small detritus into large detritus (Fennel et al., 2006), and (3) scavenging of dissolved iron onto small detritus only, as large detritus is assumed to account for a negligible fraction of total particle surface area per volume of seawater. We also replace the original Ivlev formulation of grazing with a Holling-type formulation (Fennel et al., 2006). By distinguishing large detritus (dead zooplankton, aggregated phytoplankton, and aggregated small detritus) from small detritus (dead phytoplankton), the model can treat separately the faster sinking of aggregated *P. antarctica* and large detritus and the slower sinking of small particles. Also, unlike in the original Fiechter et al. (2009) model, our model assumes that the uptake of dissolved inorganic nutrients by phytoplankton proceeds with a fixed Fe:N ratio (Table 1), given the lack of relevant observations for the ASP. In our model, the simplification is made that all dFe is available for uptake or scavenging. We do not attempt to represent explicitly dissolved Fe ligands, which are often unrealistically assigned a fixed concentration and a conditional stability constant (Matsumoto et al., 2013; Tagliabue et al., 2016). Colloidal Fe is implicitly assumed to be a component of dFe and is not treated explicitly, as no observations are available for Fe ligands or colloidal Fe in the ASP.

Scavenging rates of Fe onto particulate organic matter are set proportional to the product of small detritus and dFe concentrations. The scavenging of dFe (S, in $\mu mol\ Fe\ m^{-3}\ day^{-1}$) by small detritus is parameterized as in Aumont et al. (2015), their equation 50):

$$S = S_{SD} \times N_{SD} \times dFe, \tag{1}$$

where S_{SD} is the scavenging rate coefficient of dFe by small detritus (($mmol\ N\ m^{-3})^{-1}\ day^{-1}$), N_{SD} is the concentration of small detritus ($mmol\ N/m^{-3}$), and dFe is the dFe concentration in $\mu mol\ Fe/m^3$. Rather than using a fixed dFe scavenging coefficient at all depths (e.g., Parekh et al., 2005), this dependence of the scavenging rate on both the particle and iron concentrations is arguably a somewhat more realistic representation

Table 1
Biogeochemical Parameters of the Model

Category	Description (symbol)	Value	Range	Units
1	Nitrate uptake half-saturation constant (k_N)	2.5	—	mmol N/m^3
	Iron uptake half-saturation constant (k_F)	0.26	—	μmol Fe/m^3
	Maximum grazing rate ($G_{\max}$)	0.3	—	day^{-1}
	Sinking rate of phytoplankton (w_P)	0.05	—	m/day
	Sinking rate of small detritus (w_{SD})	0.71	—	m/day
	Fe:N ratio for phytoplankton uptake (FeN)	$2 \times 106/(16 \times 1000)$	—	μmol Fe (mmol N)$^{-1}$
2	Remineralization rate of nitrogen in large detritus (R_{LD})	0.05	—	day^{-1}
	Sinking rate of large detritus (w_{LD})	5	—	m/day
3	Maximum growth rate ($P_{\max}$)	0.82	0.82–1.79	day^{-1}
	Initial slope photosynthesis-irradiance curve (α)	0.12	0.056–0.145	(W m^{-2})$^{-1}$ day^{-1}
	Rate constant for phytoplankton mortality (m_P)	0.005	0.005–0.05	day^{-1}
	Rate of scavenging of dissolved Fe by small detritus (S_{SD})	0.03	0.005–0.1	(mmol N m^{-3})$^{-1}$ day^{-1}
	Rate of aggregation of phytoplankton and small detritus (A)	0.0014	0.001–0.01	(mmol N m^{-3})$^{-1}$ day^{-1}
	Rate of remineralization of nitrogen in small detritus (R_{SD})	0.005	0.005–0.1	day^{-1}
	Grazing half-saturation (k_P)	0.56	0.56–3.5	(mmol N/m^3)^2
	Rate constant for zooplankton mortality (m_Z)	0.14	0.025–0.25	day^{-1}
	Fraction of nitrogen excreted by zooplankton (E)	0.1	0.1–0.3	dimensionless

of surface adsorption processes in the ocean (Tagliabue et al., 2016). Desorption of Fe is not modeled explicitly, again because of a lack of relevant data, but is instead implicitly included in the process of remineralization, which transfers N and Fe (at a fixed ratio) from both large and small detritus to the dissolved pool. Other models have treated the processes of desorption and remineralization separately (Marchal & Lam, 2012). In the absence of supporting data from ASP, we do not allow Fe to cycle more rapidly than N (Rafter et al., 2017).

The governing equations of the nitrogen cycle model (Figure 2a) are (all terms in units of mmol N m^{-3} day^{-1}, with parameter definitions as in Table 1):

DIN:

$$\frac{\partial DIN}{\partial t} = -UN_P + EGN_Z + R_{SD}N_{SD} + R_{LD}N_{LD} + \frac{\partial}{\partial z} K_z \frac{\partial DIN}{\partial z} \tag{2}$$

Phytoplankton (N_P):

$$\frac{\partial N_P}{\partial t} = +UN_P - GN_Z - m_P N_P - A(N_{SD} + N_P)N_P - w_P \partial N_P / \partial z + \frac{\partial}{\partial z} K_z \frac{\partial N_P}{\partial z} \tag{3}$$

Zooplankton (N_Z):

$$\frac{\partial N_Z}{\partial t} = +GN_Z - EGN_Z - m_Z N_Z + \frac{\partial}{\partial z} K_z \frac{\partial N_Z}{\partial z} \tag{4}$$

Small detrital nitrogen (N_{SD}):

$$\frac{\partial N_{SD}}{\partial t} = +m_P N_P - A(N_{SD} + N_P)N_{SD} - R_{SD}N_{SD} - w_{SD}\partial N_{SD}/\partial z + \frac{\partial}{\partial z} K_z \frac{\partial N_{SD}}{\partial z} \tag{5}$$

Large detrital nitrogen (N_{LD}):

$$\frac{\partial N_{LD}}{\partial t} = +m_Z N_Z + A(N_{SD} + N_P)^2 - R_{LD}N_{LD} - w_{LD}\partial N_{LD}/\partial z + \frac{\partial}{\partial z} K_z \frac{\partial N_{LD}}{\partial z} \tag{6}$$

In equations (2)–(6) the term UN_P is the uptake rate of nitrate by phytoplankton, EGN_Z is zooplankton excretion, $R_{SD}N_{SD}$ is small detritus remineralization, $R_{LD}N_{LD}$ is large detritus remineralization, GN_Z is grazing,

$m_P N_P$ is phytoplankton mortality, $w_P \partial N_P / \partial z$ is phytoplankton sinking, $A(N_{SD} + N_P)N_P$ is phytoplankton aggregation, $m_Z N_Z$ is zooplankton mortality, $A(N_{SD} + N_P)N_{SD}$ is small detrital aggregation, $-w_{SD} \partial N_{SD} / \partial z$ is small detrital sinking, $A(N_{SD} + N_P)^2$ is the aggregation of phytoplankton and small detritus, and $w_{LD} \partial N_{LD} / \partial z$ is large detrital sinking. The last term of each equation is the vertical mixing term, where K_z (in m^2/s) is the vertical subgrid scale diffusivity, which is a function of time and depth in the model.

The governing equations of the iron cycle model (Figure 2b) are (all terms in units of μmol Fe m^{-3} day^{-1}):

Dissolved iron (dFe):

$$\frac{\partial dFe}{\partial t} = -UFeN \ N_P - S_{SD}N_{SD}dFe + R_{SD}Fe_{SD} + R_{LD}Fe_{LD} + \frac{\partial}{\partial z}K_z\frac{\partial dFe}{\partial z} \tag{7}$$

Living phytoplankton-associated iron (Fe_P):

$$\frac{\partial Fe_P}{\partial t} = +UFeN \ N_P - GN_Z(Fe_P/N_P) - m_P Fe_P - A(N_{SD} + N_P)Fe_P - w_P\partial Fe_P/\partial z + \frac{\partial}{\partial z}K_z\frac{\partial Fe_P}{\partial z} \tag{8}$$

Small detritus-associated iron (Fe_{SD}):

$$\frac{\partial Fe_{SD}}{\partial t} = +m_P Fe_P + S_{SD}N_{SD}dFe - A(N_{SD} + N_P)Fe_{SD} - R_{SD}Fe_{SD} - w_{SD}\partial Fe_{SD}/\partial z + \frac{\partial}{\partial z}K_z\frac{\partial Fe_{SD}}{\partial z} \tag{9}$$

Large detritus-associated iron (Fe_{LD}):

$$\frac{\partial Fe_{LD}}{\partial t} = +GN_Z(Fe_P/N_P) + A(N_{SD} + N_P)(Fe_{SD} + Fe_P) - R_{LD}Fe_{LD} - w_{LD}\partial Fe_{LD}/\partial z + \frac{\partial}{\partial z}K_z\frac{\partial Fe_{LD}}{\partial z} \tag{10}$$

In equations (7)–(10) the term $UFeN \ N_P$ is phytoplankton uptake, $S_{SD}N_{SD}dFe$ is scavenging, $R_{SD}\ Fe_{SD}$ is small detrital remineralization, $R_{LD}Fe_{LD}$ is large detrital remineralization, $GN_Z(Fe_P/N_P)$ is grazing, $m_P Fe_P$ is phytoplankton mortality, $A(N_{SD} + N_P)Fe_P$ is phytoplankton aggregation, $w_P \partial Fe_P / \partial z$ is phytoplankton sinking, $A(N_{SD} + N_P)Fe_{SD}$ is small detrital aggregation, $w_{SD}\partial Fe_{SD}/\partial z$ is small detrital sinking, $A(N_{SD} + N_P)(Fe_{SD} + Fe_P)$ is the aggregation of phytoplankton and small detritus, and $w_{LD}\partial Fe_{LD}/\partial z$ is large detrital sinking. As in the nitrogen cycle model, the last term of each equation is the vertical mixing term.

The following functional forms are assumed in the model:

Phytoplankton growth rate (U, day^{-1}), with the last term representing the photosynthesis-irradiance relationship (Evans & Parslow, 1985):

$$U = P_{\max} \times \min\left(\frac{dFe}{k_F + dFe}, \frac{DIN}{k_N + DIN}\right)\frac{\alpha I}{\sqrt{\alpha^2 I^2 + P_{\max}^2}} \tag{11}$$

Photosynthetically active radiation (I, W/m^2):

$$\frac{\partial I}{\partial z} = -k_d\ I \tag{12}$$

Light attenuation (k_d, m^{-1}; Fasham et al., 1990):

$$k_d = 0.04 + 0.040 \times N_P \tag{13}$$

Grazing rate (G, day^{-1}):

$$G = G_{\max}\frac{N_P^2}{k_P + N_P^2} \tag{14}$$

In equations (2)–(14), all variables not listed as prognostic (state) variables are model parameters defined in Table 1.
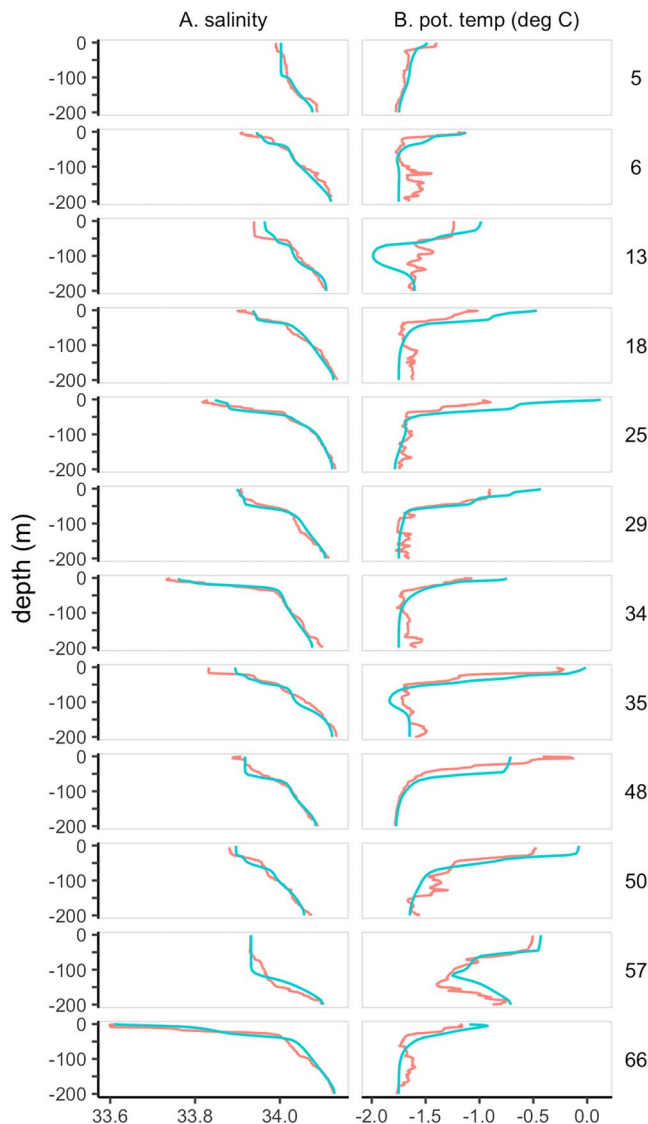
Figure 3. Vertical profiles of (a) salinity and (b) potential temperature for the model (green) and Amundsen Sea Polynya International Research Expedition (ASPIRE) observations (orange) at the 12 ASPIRE stations. The model is sampled at the same dates the stations were visited during ASPIRE.

2.4. Model Forcing

Surface forcing for the model (1 October 2010 to 31 March 2011) includes (1) zonal and meridional wind speed, (2) sea ice concentration, (3) incoming shortwave radiation, (4) surface air temperature, (5) net surface longwave radiation, and (6) sea ice meltwater contribution at the location of each station. The wind speed and direction come from the Antarctic Mesoscale Prediction System (Powers et al., 2012) and have 3-hr resolution (see Figure S1 in the supporting information showing a reasonably good comparison with winds observed from the ship during ASPIRE). The wind speed values used in our model calculations are adjusted for sea ice cover by assuming that the squared wind speed (proportional to surface stress) is proportional to sea ice concentration (i.e., zero speed for a full ice cover). To this end, we use observed sea ice concentration (SIC) from the local ASMR-E sea ice concentration (Cavalieri et al., 2014). The incoming shortwave radiation is from the European Centre for Medium-Range Weather Forecasts Reanalysis Interim (ERA-Interim) reanalysis (Dee et al., 2011, 3-hourly) and is multiplied by $(1 - \text{SIC})$ to account for sea ice cover. Surface air temperature and net longwave radiation are from ERA-Interim (monthly resolution) and are prescribed over open water (SIC = 0), while values of -1.8 C and 0 W/m^2 (respectively) are assumed during a full ice cover (SIC = 1). A weighted average of those two extremes is used when $0 < \text{SIC} < 1$ (corresponding to the case of a grid cell that is partially covered by sea ice). Finally, a surface freshwater contribution is included to represent the effect of sea ice melt between 1 October and 1 January, during which the polynya transitions from closed to open (Mu et al., 2014; Stammerjohn et al., 2015). For simplicity, the flux is assumed constant over this period and, given the absence of data, it is adjusted for each station (by trial and error) to maximize agreement with the observed salinity profile once the model reaches the calendar date at which ASPIRE observations were made (Figure 3). This freshwater contribution, cumulated between 1 October and 1 January, varies between 0 and 0.27 m of meltwater, depending on station. This represents a small fraction of the typical sea ice thickness in the Amundsen Sea (~1.5 m in winter; Kurtz & Markus, 2012; Xie et al., 2013) and is consistent with the observations that the ASP is primarily formed by winds (Stammerjohn et al., 2015) and dominated by sea ice production over sea ice melt (Randall-Goodwin et al., 2015). The model uses bulk formulas (Fairall et al., 2003) to derive surface wind stresses and surface heat fluxes from the observations described above. The model does not account for evaporation and precipitation at the surface and assumes that vertical wind mixing is the only process influencing salinity after 1 January. The assumption behind this approximation is that evaporation and precipitation play a much smaller role than does sea ice melt (whose parameterization is described above) and can be neglected for simplicity. For example, reanalysis products suggest that precipitation and evaporation represent a freshwater net input of ~1.5 mm/day in the Amundsen Sea (Grieger et al., 2016, their Figure 1). The model considers the bottom as a solid boundary (i.e., the vertical fluxes are zero) with the exception of sinking particles (detritus, living phytoplankton). Sinking particles pass through the bottom boundary as if the water column continued beyond 210-m depth.

The photosynthetically active radiation (PAR) immediately above the sea surface (denoted as 0^+) is assumed to be proportional to the 3-hourly surface downwelling shortwave radiation of ERA-Interim (SW). With 3-hourly PAR values, the model simulates the diurnal cycle. Ship observations collected during ASPIRE suggest that PAR ≈ 0.64 SW, the proportion assumed in our study. Vertical PAR profiles (84 profiles) collected during the same cruise suggest that PAR immediately below the surface (0^-) can be approximated as $\text{PAR}(0^-)/\text{PAR}(0^+) \approx 0.84 - 0.0071 \times \text{zeni}$, where zeni is the solar zenith angle. The same PAR profiles are

combined with observed profiles of chlorophyll (converted to nitrogen assuming a mass ratio C:Chl = 50 and Redfield C:N) to derive a parameterization of the light attenuation coefficient (k_d, in m^{-1}) due to phytoplankton self-shading (see section 2.3, equation (13)).

2.5. Model Initialization

Initial temperature-salinity profiles are taken as different among the 12 stations. No temperature and salinity data were available for 1 October 2010 (when the simulations begin), and thus, these initial profiles have to be generated from other data (15 December 15 to 9 January 2010 depending on the station; see Yager et al., 2016). Conditions below 100 m are assumed to be identical to those at the time of ASPIRE. Above 100 m, salinity and temperature are assumed to vary linearly with depth until they reach surface values chosen (by trial and error) to maximize agreement with the data once the model reaches the time period of the ASPIRE field measurements (Figure 3). We note that because ROMS is limited in that the biogeochemistry cannot affect the physics, the modeled evolution of the temperature profile does not take into account the potential effects of reduced shortwave light penetration due to high biomass in the mixed layer (the model assumes a constant absorption coefficient).

Initial concentrations of DIN and dissolved Fe are taken as uniform throughout the water column and for all stations and are set at their estimated winter water concentrations: DIN = 31 mmol/m^3 (Yager et al., 2016) and dFe = 0.3 ± 0.05 μmol/m^3 (Sherrell et al., 2015). The initial concentrations of the other pools are set to low values: 10^{-3} mmol N/m^3 for all other nitrogen pools and 10^{-3} μmol Fe/m^3 for all other iron pools.

2.6. Biogeochemical Model Parameters

The model includes 18 biogeochemical parameters (Table 1), which can be divided into the following three categories: (1) parameters constrained by previous studies on *P. antarctica* or biogeochemical cycling in the ASP, (2) parameters that can be derived from the ASPIRE data set, and (3) poorly constrained parameters.

Parameters falling into Category 1 include (1) the half-saturation constant for nitrate uptake by colonial *P. antarctica* (k_N, 2.5 mmol N/m^3, Wang & Moore, 2011), (2) the half-saturation constant for Fe uptake by colonial *P. antarctica* (k_F, 0.26 μmol Fe/m^{-3}, Garcia et al., 2009), (3) the maximum grazing rate of microzooplankton (G_{max}, 0.3 day^{-1}, Yang et al., 2016), (4) the sinking rates of colonial *P. antarctica* (w_P, 0.05 m/day^1, Becquevort & Smith, 2001) and small detritus (w_{SD}, 0.71 m/day, Becquevort & Smith, 2001), and (5) the Fe:C ratio for *P. antarctica* uptake (2 μmol Fe (mol C)$^{-1}$, Strzepek et al., 2011, 2012, Figure S2 in the supporting information).

Though significantly lower half-saturation constants for Fe uptake have been observed for (likely) solitary *P. antarctica* in the Ross Sea (Coale et al., 2003), relatively high half-saturation constants have been measured for colonial *P. antarctica* living under light-limited conditions (Garcia et al., 2009; Sedwick et al., 2007). Given that colonial *P. antarctica* were dominant during ASPIRE (Yager et al., 2012; Hyun et al, 2016) and were likely experiencing significant light limitation (Schofield et al., 2015), we selected the larger half-saturation constant for Fe uptake of Garcia et al. (2009).

The final Category 1 parameter is the Fe:C ratio. Given the iron limitation observed during ASPIRE (Alderkamp et al., 2015), we select a Fe:C ratio determined for *P. antarctica* growing under iron-limiting conditions (Figure S2 in the supporting information). Assuming Redfield stoichiometry (C:N = 6.625, Redfield, 1963), we use this Fe:C ratio to derive the Fe:N ratio for phytoplankton uptake (Fe: N = 0.013 μmol Fe (mmol N)$^{-1}$).

Category 2 parameters derived from ASPIRE observations (Yager et al., 2016) include the remineralization rate of nitrogen in large detritus (R_{LD}, 0.05 day^{-1}) and the sinking rate of large detritus (w_{LD}, 5 m/day), which are determined from data from drifting sediment traps deployed at 60 and 150 m during ASPIRE (Yager et al., 2016).

The remaining nine parameters (Category 3) have a large observed range (e.g., photosynthesis-irradiance curve parameters α and P_{max}; Table 1), have limited constraints from available measurements (e.g., dFe scavenging and remineralization rates), or have not been measured in the ASP, (e.g., grazing half-saturation concentration and the zooplankton mortality rate).

The scavenging rate coefficient of dissolved iron onto small detritus, S_{SD} (equation (1)), is particularly critical, given that the nonbiological process of scavenging can reduce dFe available for phytoplankton growth (Figure 2b). The possible range of values is large (Tagliabue et al., 2016). Recent estimates of vertical particulate Fe flux, a partial function of scavenging rate, show variations of at least a factor of 2, depending on the method used to estimate the flux (Hayes et al., 2018). Aumont et al. (2015) suggested a value of 0.005 $(\mu mol\ C\ L^{-1})^{-1}\ day^{-1}$, where scavenging rate is dependent on the product of dFe and particle concentration in units of particulate organic carbon. We have employed this rate coefficient, equivalent to 0.033 $(mmol\ N\ m^{-3})^{-1}\ day^{-1}$ for our model, assuming a C:N molar ratio of 6.6 (Redfield, 1963; Yager et al., 2016).

In this study, we are interested to see what ranges of Category 3 parameter values could reproduce the observations made in the ASP and to determine parameters to which the model output is most sensitive. We test a large range of these parameters to find a set of values that is both realistic and most consistent with ASPIRE observations. We also explore relationships among the model parameters in the process.

2.6.1. Model-Data Comparison: The Cost Function

We formulate a cost function to estimate values of model parameters that lead to the best fit to the observations. The cost function is a weighted sum of squared differences between the model output and field observations. A lower value of the cost function indicates a better fit of the model to the observations. An optimal set of parameter values is thus obtained when the cost function is minimized.

The observations used in the cost function are concentrations of DIN and dFe collected between the surface and 200 m at 12 stations occupied during ASPIRE (the same observations were used by Yager et al., 2016, not including Station 68). Observations from these stations span 14 December 2010 to 5 January 2011, covering the beginning and rise of the bloom. We determined DIN to be the most important variable to include in the cost function, because the differences in DIN between stations were used as the primary indicator of bloom progression in Yager et al. (2016). Since DIN values at each depth and station strongly correlated negatively with particulate organic nitrogen (PON; $R = -0.96$; $n = 85$; $p < 0.01$) and with Chl a ($R = -0.90$; $n = 86$; $p < 01$; Yager et al. (2016)), we find that including PON and Chl a in the optimization (section 2.6.2) effectively overweights DIN, resulting in a very close fit to observed DIN, but a poorer fit to dFe. Therefore, we do not include PON and Chl a in the calculation of the cost function to ensure the equal weighting of Fe and nitrogen. We note that an initial optimization that included all four variables did not produce very different results.

Our cost function (J) is a simplified version of that considered by Friedrichs et al. (2007):

$$J = \frac{1}{M} \sum_{m=1}^{M} \frac{\left(\frac{1}{\sigma_m}\right)^2}{N_m} \sum_{j=1}^{N_m} \left(a_{jm} - \widehat{a}_{jm}\right)^2 \tag{15}$$

where M is the number of observation types, σ_m is the error of the observation type m, N_m is the total number of observations of type m, a_{jm} is the modeled value, and $\widehat{a}_{jm}$ is the measured value.

2.6.2. Optimization Algorithm

Running the model over several stations to calculate the cost function during parameter tuning is a time-intensive process. High computational time is required for each cost function calculation, which must be carried out for each change in a Category 3 parameter value. Therefore, derivative-based numerical optimization algorithms that require many cost function calculations do not minimize the cost function efficiently. Instead, we use Bayesian optimization, a global optimization algorithm that does not require derivatives (Mockus, 1989). Bayesian optimization is best suited for optimizing computationally expensive functions, like the cost function used in this study. For the Bayesian optimization algorithm, previous data about the behavior of the cost function (the prior) is used to estimate the parameters that will result in the largest expected decrease of the cost function (Snoek et al., 2012). With the first iterations, the prior is treated as a random function. With each iterative calculation of the cost function, the algorithm updates its prior and incorporates the new prior into the next estimate of best parameter values. This Bayesian approach determines simultaneously the best values of parameters that minimize the cost function, with fewer calculations of the cost function than a derivative-based optimization approach.

The optimization algorithm iteratively tests different sets of parameter values, within imposed inequality constraints for each (Table 1) and is applied at 9 of the 12 ASPIRE stations (retaining three stations to test
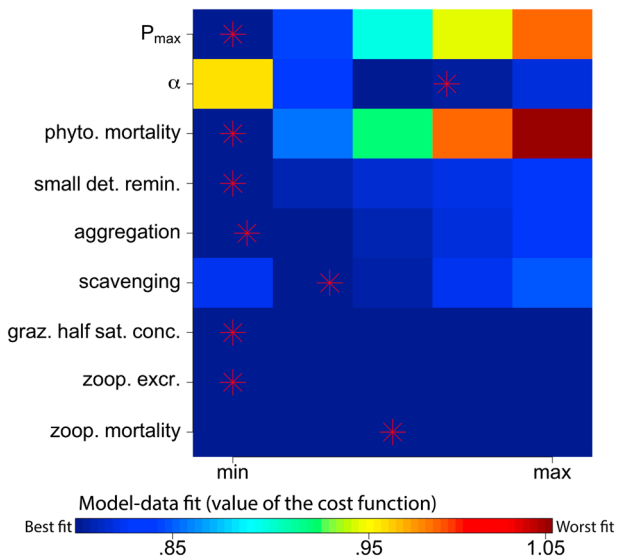
Figure 4. Values of the cost function from rerunning the model at the nine stations used for optimization while varying Category 3 biogeochemical parameters, one at a time (Table 1). On top, red asterisks indicate the values of the optimized parameters (the "Final values" listed in Table 1; see section 2.6.2). Blue = low cost function value (best fit); red = high cost function value (worst fit). The color scale is on a $\log_{10}$ scale, to help highlight small differences between shades of blue.

model accuracy after optimization; see below) using the new set of parameters before calculating the cost function. This process continues for a prespecified number of iterations. The set of parameter values from the iteration leading to the minimum cost function value is then designated as the "optimized values." Though we choose to run the optimization for 100 iterations, the optimized parameter values are reached after 50 iterations typically.

We optimize nine Category 3 parameters (Table 1): (1) the initial slope of the photosynthesis-irradiance curve (α), (2) the maximum uptake rate of DIN (P_{max}), (3) the phytoplankton mortality rate constant (m_P), (4) the scavenging rate constant (S_{SD}), (5) the aggregation rate constant for phytoplankton and small detritus (A), (6) the remineralization rate constant for nitrogen and iron present in small detritus (R_{SD}), (7) the half-saturation constant for zooplankton grazing (k_P), (8) the zooplankton excretion rate constant (E), and (9) the zooplankton mortality rate constant (m_Z). Upper and lower parameter bounds of α and P_{max} are determined from the range of values reported for *P. antarctica* (Alderkamp et al., 2015). Given that averaged stoichiometric ratios during ASPIRE indicated a high proportion of living cells (Yager et al., 2016), we assume that the phytoplankton mortality rate (m_P) would not exceed 0.05 day^{-1}. Ranges covering several orders of magnitude are used for S_{SD}, A, D, and R_{SD} to explore a wide parameter space (Table 1). For the zooplankton parameters k_P, m_Z, and E, we assume ranges from previous modeling studies (Fennel et al., 2006, for k_P and m_Z, and Fennel et al., 2006, and Fiechter et al., 2009, for E).

To check that the optimization yields parameter estimates that could be applied at stations where model results are not constrained by observations, three stations are excluded from optimization: (1) Station 6, with a shallow mixed layer, (2) Station 13, with a deep mixed layer, and (3) Station 50, with a mixed layer depth that is typical of most polynya stations (Figure 1). By testing the model-data fit at these three stations, we could assess whether the optimized values are applicable at stations for which data have not been assimilated (Friedrichs et al., 2007).

We evaluate the uncertainty of the optimized parameters by rerunning the model at the nine stations used for optimization while varying the parameters relative to their optimized values, one at a time. We vary each of the nine Category 3 parameters at five equally spaced values between the upper and lower parameter bounds (45 total runs). Figure 4 shows the outcome of the cost function for each of these runs. We use this same method, except varying parameters two at a time rather than just one at a time, to evaluate how the cost function changes when varying two parameters together through both of their ranges (Figure 5). We exclude the parameters that did not significantly influence the cost function (Figure 4, solid blue rows) from this pairwise analysis. We find that optimized parameter values coincide with those at which the cost function is lowest in both of these exercises, so we are satisfied with the outcome of the optimization.

2.6.3. Accounting for Uncertainty in Remaining Unconstrained Parameters

Some parameters did not significantly influence the cost function (Figure 4, blue solid rows) and therefore cannot be constrained by the optimization procedure. The main reason certain parameters cannot be constrained by the optimization is presumed to be because the ASPIRE data only cover the first half of the bloom. While these parameters do not influence the model fit to DIN and dFe data from December and early January, they may influence the later part of the bloom, the timing of which is documented by remote sensing data (Arrigo et al., 2012). To constrain the remaining parameters, we use a Latin hypercube analysis (Stein, 2012), which is more efficient computationally than a Monte Carlo analysis (Helton & Davis, 2003). For this analysis, three values (minimum and maximum [Table 1] and midrange) of these parameters are run for all 12 ASPIRE stations with the rest of the parameters held at their constrained or optimal values, totaling to 27 (3^3) additional model runs for each station. By excluding parameterizations that result in
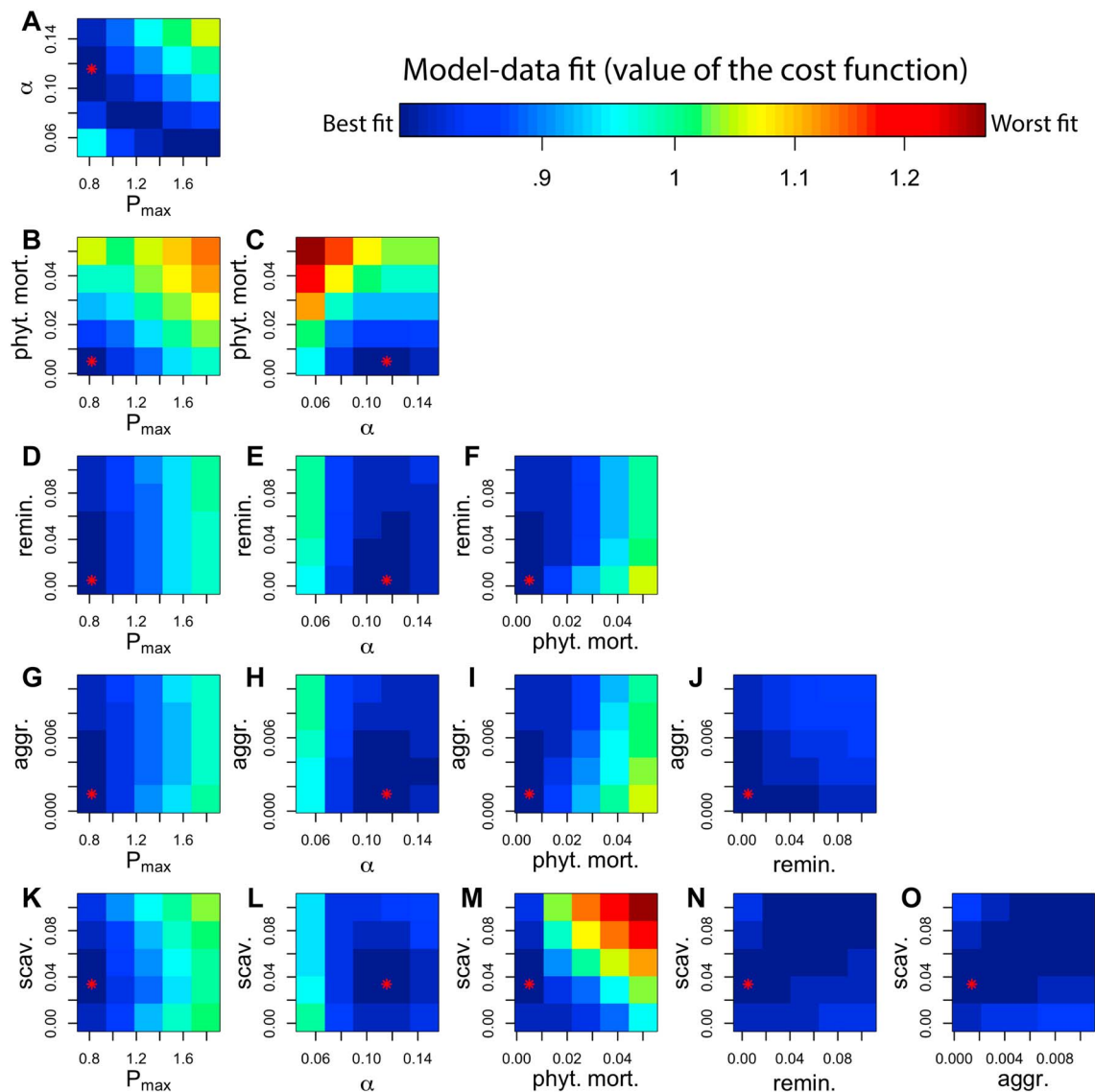
Figure 5. Values of the cost function from rerunning the model at the nine stations used for optimization while varying Category 3 parameters, two at a time (Table 1). Each subplot is labeled on its *x* and *y* axis by the names and values of the two parameters being adjusted for each calculation of the model-data fit (the cost function). Dark blue squares indicate a lower cost function value (stronger model-data fit), and red squares indicate a higher cost function value (weaker model-data fit). Red asterisks indicate optimized parameter values ("Final values" listed in Table 1; see section 2.6.2); thus, a red asterisk on a dark blue box indicates that the optimized model provides the best fit to the data when two parameters are varied simultaneously. The color scale is on a $\log_{10}$ scale, to help highlight small differences between shades of blue.

unrealistic bloom ending dates (defined as the last date with average surface Chl $a \geq 1$ mg/m^3), we narrow down possible values of these remaining poorly constrained parameters.

Of the 27 combinations of parameters tested in the Latin hypercube analysis, only one results in an average bloom ending date (all stations except marginal ice zone Station 66) within a week of that observed by satellite remote sensing for the polynya region (Arrigo et al., 2012). The combination of parameters that results in a modeled bloom end date closest to the observed end date (23 February ±5 days) is designated as the optimized parameter set (red asterisks in Figures 4 and 5).

2.7. Low Winter dFe Scenario

Using the optimized parameter set, we also test the model with a hypothetically low winter concentration of dFe, which would be the concentration predicted if there were no "meltwater pump" bringing dFe

from either glacial meltwater, circumpolar deep water, or the sediments to the upper 200 m of the polynya (St-Laurent et al., 2017). For this scenario, we lower the initial dFe concentration from 0.3 to 0.1 μmol/m^3. We select 0.1 μmol/m^3 for the winter dFe concentration for this scenario since this approximates the lowest dFe concentration observed in subsurface waters during ASPIRE (Sherrell et al., 2015, e.g., Station 57.04 at 100 m).

2.8. Definitions

For the sake of clarity, we will use the term "model-data fit" instead of "cost function" for the remainder of this paper.

We define the model-data difference in depth-integrated (0–100 m) net community production (NCP difference, mol C/m^2) as the model-data difference in DIN drawdown at the dates of ASPIRE sampling over the upper 100 m between model and observations, multiplied by the C:N molar ratio of 6.6 (Redfield, 1963; Yager et al., 2016).

Integrated gross primary production (GPP, in mmol C m^{-2} day^{-1}) is defined as

$$GPP = \int U \times N_P \times C:N \, dz \tag{16}$$

where U is the phytoplankton growth rate from equation (11), N_P is the concentration of nitrogen in the phytoplankton pool, and C : N is the carbon:nitrogen ratio, assuming Redfield stoichiometry (C:N = 6.6, Redfield, 1963). The vertical integral is over the top 210 m of the water column.

We use the terms from the uptake rate calculation from equation (11) to assess quantitatively the light and nutrient limitation and availability. Mixed-layer DIN concentrations observed during ASPIRE were always greater than 3 times k_N, suggesting no nitrogen limitation during the first half of the bloom. The model showed no N limitation either $\left(\frac{DIN}{k_N + DIN} \sim 1\right)$ so we will discuss limitation in terms of light and iron only, not DIN, for the remainder of the article.

Light availability varies between 0 (not available) and 1 (saturating) and is defined as

$$light\ availability = \frac{\alpha I}{\sqrt{\alpha^2 I^2 + P_{max}{}^2}} \tag{17}$$

with photosynthetic parameters α and P_{max} as defined in Table 1 and I (the photosynthetically active radiation) as defined by equation (12).

Light limitation varies between 0 (saturating) and 1 (not available) and is defined as

$$light\ limitation = 1 - light\ availability \tag{18}$$

Iron availability varies between 0 (not available) and 1 (replete) and is defined as

$$iron\ availability = \frac{dFe}{k_F + dFe} \tag{19}$$

where dFe is the concentration of dFe and k_F is the half-saturation constant (Table 1). Note that given our chosen values of k_F = 0.26 μmol Fe/m^3 (see section 2.6) and initial winter dFe concentration of 0.3 μmol Fe/m^3 (see section 2.5), iron availability does not exceed 50% of replete concentrations.

Iron limitation varies between 0 (not limiting) and 1 (not available) and is defined as

$$iron\ limitation = 1 - iron\ availability \tag{20}$$

In the absence of a detailed colimitation analysis (e.g., Saito et al., 2008) in the ASP, we assume that light and iron limitations are multiplicative. Total availability varies between 0 (no light or dFe available) and 1 (saturating light and replete dFe) and is defined as

$$total\ availability = light\ availability \times iron\ availability \tag{21}$$

AGU
100
ADVANCING EARTH
AND SPACE SCIENCE

Global Biogeochemical Cycles

10.1029/2018GB006168

This approach may overestimate the total limitation because most phytoplankton cells adjust their iron demand in response to light availability.

When reporting a statistic across multiple stations, results are reported as the mean ±1 standard deviation. Results from Station 66 are considered as representative of a "marginal ice zone." All other locations are considered "within the polynya."

The mixed layer depth (MLD) is defined as the depth of the maximum buoyancy frequency (Carvalho et al., 2017), which should reflect the halocline depth in the early bloom and the thermocline or halocline depth later in the season.

Vertical carbon flux is defined as that arriving at 100 m, when we are not comparing modeled vertical carbon flux to ASPIRE observations of vertical carbon fluxes at 60 and 150 m. We define total seasonal (6-month) vertical carbon flux as the cumulative vertical carbon flux at 100 m over the entire modeled period (from 1 October 2010 to 31 March 2011). The vertical carbon flux includes small detritus, large detritus, and living phytoplankton.

3. Results

3.1. Model-Data Fit Sensitivity

The optimization using dFe and DIN data from APSIRE successfully constrains most of the parameters from Category 3 with the exception of the zooplankton parameters (Figure 4). The model-data fit is best with low values of P_{max}, phytoplankton mortality, small detritus remineralization, and aggregation, and moderate values of α and the scavenging rate constant. The optimized value of the scavenging rate constant is very close to that suggested by Aumont et al. (2015). The three zooplankton parameters have little to no effect on the model-data fit and therefore are constrained by bloom ending date only.

Overall, the model-data fit is more sensitive to phytoplankton growth and mortality parameters than to the aggregation, scavenging, and remineralization rates (Figures 4 and 5). The photosynthesis-irradiance curve parameters α and P_{max} strongly influence the model-data fit: high α values result in low cost function values when paired with low P_{max} values and low α values result in low cost function values when paired with high P_{max} values (Figure 5a). Choice of α and P_{max} is also sensitive to the phytoplankton mortality rate, since low mortality constants result in a better model fit when combined with low P_{max} (Figure 5b) and high α (Figure 5c). In contrast, aggregation, remineralization, and iron scavenging influence the model-data fit more weakly, with relatively wide ranges of values resulting in small variations in the model-data fit (Figures 5d–5o). Narrower ranges of these three parameters result in good model-data fit under higher phytoplankton mortality, however. With a high phytoplankton mortality constant, higher remineralization (Figure 5f), higher aggregation (Figure 5i), and lower scavenging (Figure 5m), a better agreement of the model with the data is obtained.

3.2. Model-Data Comparisons

After parameter optimization, the 1-D model largely captures the observed patterns in DIN, Chl a, and PON, and to a lesser extent dFe at the stations used for data assimilation during optimization (Figures 6a–6d). Average model-data differences were 0.1 ± 3.0 mmol DIN/m^3, 1.8 ± 4.8 mg Chl a/m^3, 1.7 ± 2.5 mmol PON/m^3, and 0.03 ± 0.10 μmol dFe/m^3, with standard deviations <30% of maximum model output values. The modeled mixed layer concentrations of dFe are generally higher than observed concentrations (Figure 6a), suggesting biological drawdown and/or scavenging are underestimated. For stations where, and times when, DIN > 20 mmol/m^3, the model performs well but it is unable to reproduce the very lowest DIN concentrations observed at Station 35 (Figure 6b).

The model generally performs equally well for the three stations not included in the optimization (Figures 6e–6h). At these stations, model results differ from observations by −0.2 ± 3.3 mmol DIN/m^3, 2.5 ± 5.2 mg Chl a/m^3, and 2.7 ± 2.8 mmol PON/m^3. The model performs somewhat better for dFe for these three stations than for the stations used in the optimization (Figure 6e), and modeled dFe differs from observed values by 0.03 ± 0.07 μmol/m^3. The better model performance at these stations may result from there (accidentally) being fewer observations from the modeled nutricline, where the model-data fit for the nine stations used for optimization is rather poor (Figure 7a).
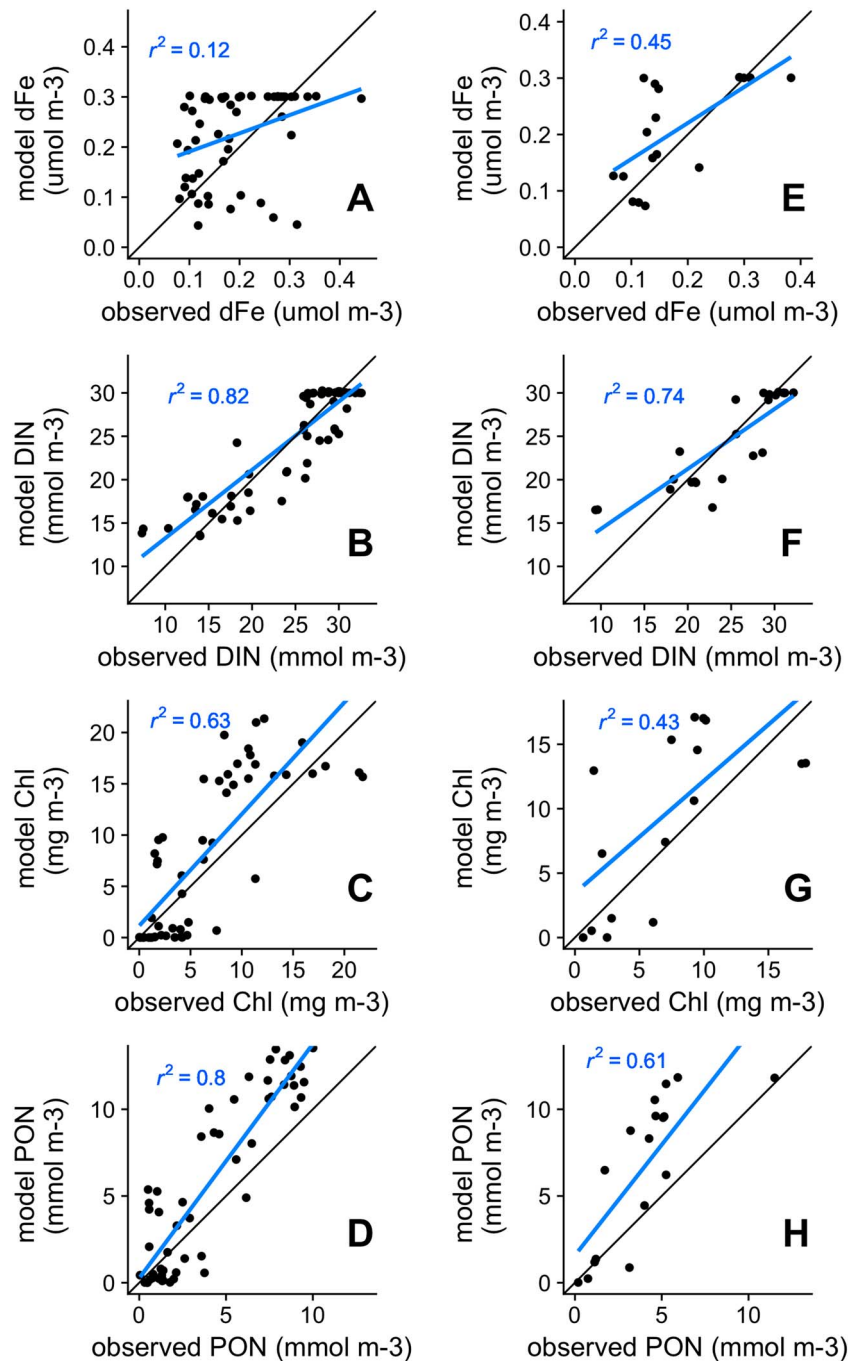
Figure 6. Comparison of model results with observations at the nine stations used for parameter optimization (left column) and at Stations 6, 13, and 50 whose data are not considered for parameter optimization (right column). Blue lines show the linear regression (r^2 is the squared Pearson correlation coefficient), and black lines are lines of perfect agreement. DIN = dissolved inorganic nitrogen; PON = particulate organic nitrogen.

At the surface, when modeled DIN concentrations are overestimated, dFe concentrations are underestimated (Stations 5, 57, and 13, see Figures 7a and 7b). The model does not capture the finer details of observed dFe vertical profiles (Figure 7a), despite reproducing observed DIN (Figure 7b), Chl *a* (Figure 7c), and PON (Figure 7d) reasonably well at most stations. Modeled nutriclines also tend to be "sharper" than observed, especially for dFe. Modeled dFe concentrations below the nutricline are generally too high (Figure 7a), contrasting with DIN vertical profiles, which reproduce ASPIRE profiles relatively well (Figure 7b).
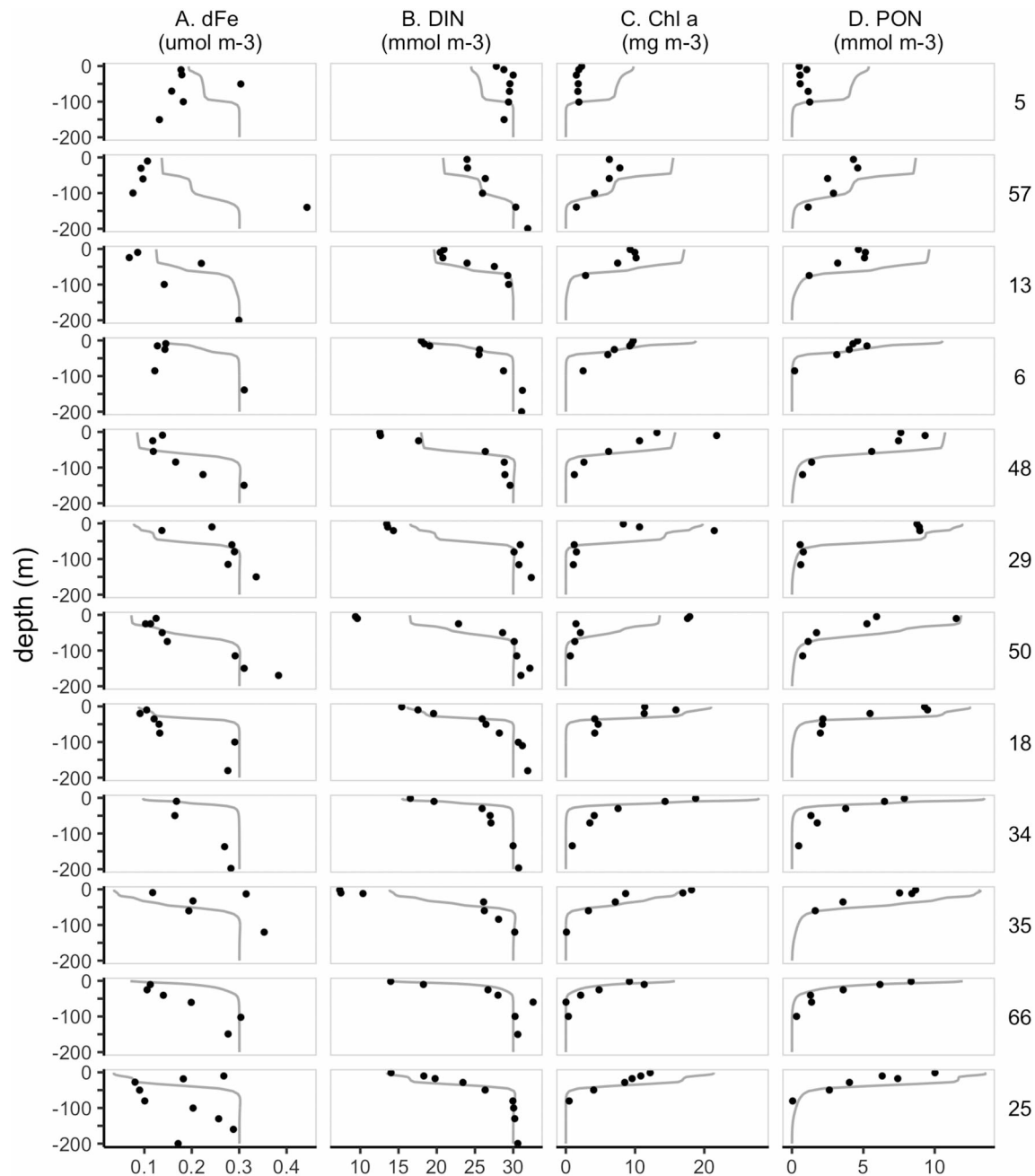
Figure 7. Vertical profiles of (a) dissolved iron (dFe), (b) dissolved inorganic nitrogen (DIN), (c) Chl *a*, and (d) particulate organic nitrogen (PON), observed (solid circles) and modeled at the time of sampling (gray lines) at each of the 12 Amundsen Sea Polynya International Research Expedition (ASPIRE) stations (the numbers on the right are station numbers). The profiles are ordered by increasing modeled surface DIN drawdown.

Despite its importance to phytophysiology (Carvalho et al., 2017), the depth of the mixed layer does not appear to influence the model-data fit. Model-data Chl *a* and DIN differences are relatively small across stations with both shallow (Stations 66, 6, and 34) and deep (Stations 29 and 57) MLDs. The most notable exception is Station 5, which is very close to the Getz Ice Shelf (Figure 1). At the time of ASPIRE sampling of Station 5, only the first hints of the bloom were observed, while in our model the bloom is already well underway by this time, driving large model-data differences of dFe, Chl *a*, DIN, and PON.

We also examine whether there exists a spatial pattern to the model-data NCP differences (Figure 8). While the NCP difference is significantly ($p < 0.05$) correlated with latitude (higher difference closer to continent;
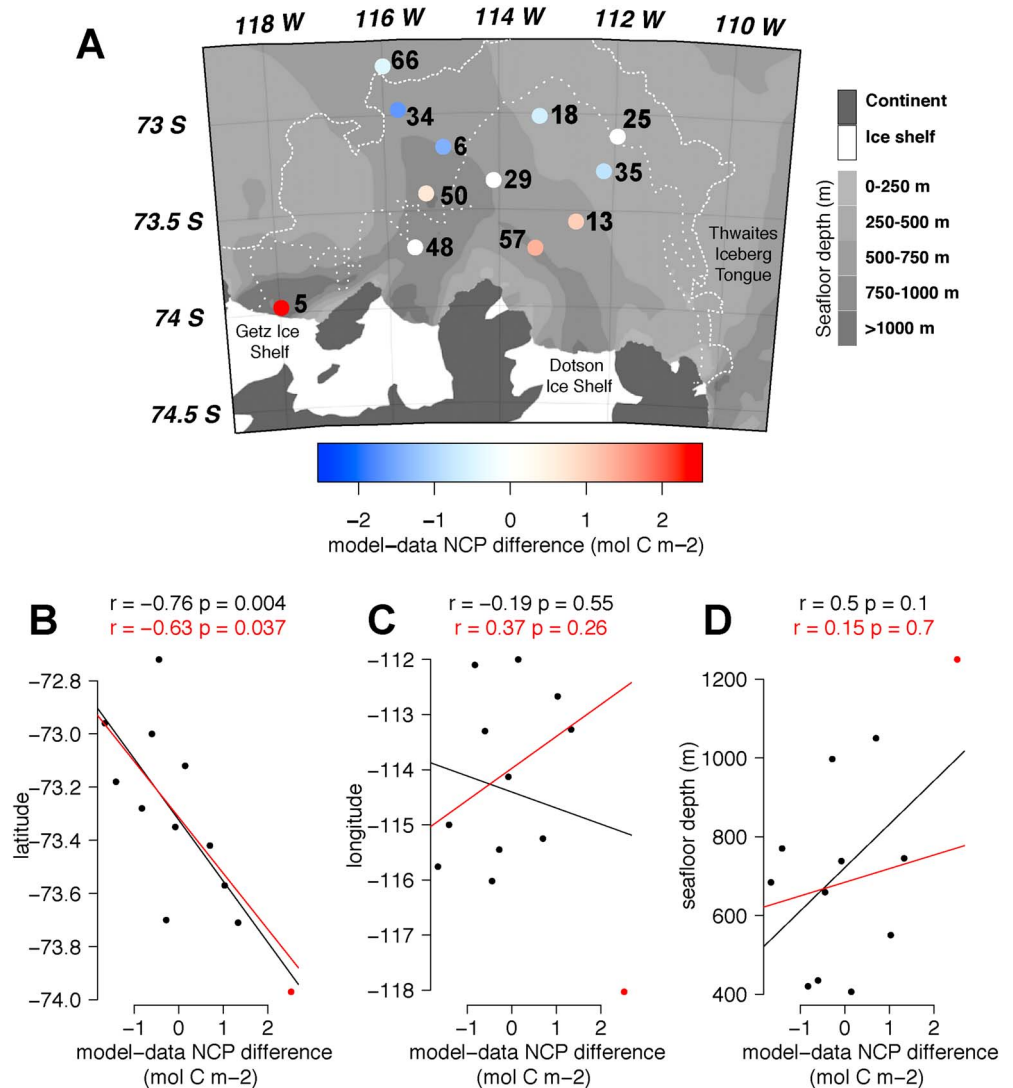
Figure 8. Geographic map of the ASP with stations colored by the mean model-data NCP differences, and scatterplots of model-data NCP differences against station latitude (b), longitude (c), and seafloor depth (d). In (a), red indicates an overestimate of NCP by the model relative to the data and blue indicates an underestimate. Black indicates the linear regressions and Pearson correlation coefficients and *p* values for all stations, and red indicates the linear regressions and Pearson correlation coefficients and *p* values for all stations, except for Station 5 (indicated in red). NCP = net community production; ASP = Amundsen Sea Polynya.

Figure 8b), neither longitude (Figure 8c) nor seafloor depth (Figure 8d) appears to influence significantly the degree to which modeled NCP matches observations. When excluding Station 5, where the NCP difference is very large due to overestimated modeled primary production, the *p* values of the Pearson correlations are affected, though the NCP difference remains significantly correlated with latitude, and not significantly correlated with longitude or seafloor depth (red versus black lines in Figure 8).

We note that the model's range of integrated primary production over the annual cycle for the 12 stations (40–210 gC m^{-2} year^{-1}) compares well with the satellite observations (30–140 gC m^{-2} year^{-1}; Yager et al., 2012, their Figure 3)

Observations of vertical carbon fluxes at 60 and 150 m from floating sediment traps have an estimated error of a factor of 2 (Yager et al., 2016). We find that the modeled vertical carbon flux is within a factor of 2 of the four ASPIRE flux estimates (based on sediment trap data). The modeled flux differs from the other two ASPIRE flux estimates by more than a factor of 2: the model overestimates the 150-m

Table 2
Model-Data Vertical Carbon Flux Comparison

Station	Depth (m)	Observed vertical carbon flux (mmol C m^{-2} day^{-1})	Modeled vertical carbon flux (mmol C m^{-2} day^{-1})
35	60	18.0	30.4
	150	3.0	6.4
57	60	27.0	10.9
	150	2.7	2.3

Note. Modeled vertical carbon fluxes shown are averaged over the same period that Amundsen Sea Polynya International Research Expedition floating sediment traps were deployed (see Yager et al., 2016, for additional information on the observed vertical carbon flux data).

vertical C flux at Station 35 by 113% and underestimates the 60-m vertical carbon flux at Station 57 by 60% (Table 2).

3.3. Controls on Bloom Initiation and Development

According to the model, the start date of the bloom (defined as the first day when surface Chl *a* reaches 1 mg/m^3) averaged over all stations is 23 November 2010 ($\pm$9 days), with light limitation sharply relieved at the time of sea ice opening (Figures 9a and 9c, and S3a and S3c in the supporting information). Once relieved from light limitation (Figure 9c), GPP increases to its seasonal maximum of 274 $\pm$ 61 mmol C m^{-2} day^{-1}, 13 $\pm$ 4 days after the bloom start date (Figures 9b and S3b in the supporting information). The rapid increase in surface Chl *a* concentration causes severe self-shading, however, and the euphotic depth shoals by 78 $\pm$ 14 m within 2 weeks of bloom initiation (Figures 9d and S3d in the supporting information). Despite intense self-shading, phytoplankton biomass continues to increase after the peak in integrated GPP.

At most stations (except the marginal ice zone, where mixed layers are very shallow at the beginning of the bloom), the euphotic depth quickly becomes shallower than the mixed layer depth in the early days of the bloom (Figures 9d and S3d in the supporting information). This is a consequence of phytoplankton self-shading. When the euphotic depth is shallower than the mixed layer depth, some proportion of phytoplankton in the surface mixed layer can be mixed below the depth of 1% incident light. This causes phytoplankton to become strongly light-limited (Figures 9c and 9d, and S3c and S3d in the supporting information). The euphotic depth becomes shallower than the mixed layer depth for the first time on 27 November 2010
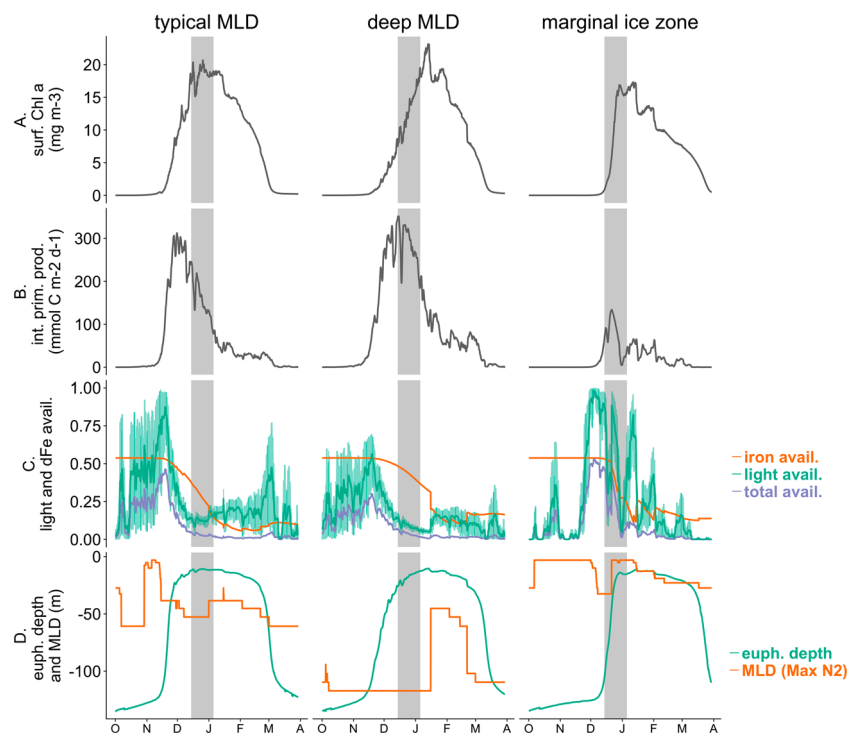

Figure 9. Time series (1 October 2010 to 31 March 2011) of variables simulated at three example stations: (a) surface Chl *a*, (b) integrated gross primary production (see equation (16) in section 2.8), (c) light, iron, and combined light and iron availability (see equations (17), (19), and (21) in section 2.8) in the mixed layer, and (d) euphotic depth and mixed layer depth. Left column: Station 29 with MLD typical for the polynya; middle column: Station 57 with a deep MLD; and right column: Station 66 with a shallow mixed layer depth (marginal ice zone). The green shaded regions in each panel in (c) shows the light saturation at the 10% and 90% daily light levels. The vertical gray bars show that the period Amundsen Sea Polynya International Research Expedition (ASPIRE) data are available. MLD = mixed layer depth.

($\pm$9 days), not long after the bloom begins (Figures 9d and S3d in the supporting information). Despite the high primary production in the first days of the bloom, dFe is only drawn down by 0.05 ± 0.04 nmol/m^3 before the euphotic depth becomes shallower than the mixed layer depth, and so light is more limiting than iron for the bloom in the mixed layer.

According to the model results, this rapid onset of self-shading and light limitation is more extreme under weaker stratification, such as at Station 57. Here the euphotic depth becomes shallower than the mixed layer depth at about the same time as the bloom start date and remains so for most of the rest of the modeled period (Figure 9d). Under the much more highly stratified conditions at the marginal ice zone, however, the mixed layer depth remains shallower than the euphotic depth despite rapid increases in surface Chl a. Here the mixed layer is shallower than in the central polynya, and iron limitation in the mixed layer can impose itself more rapidly as long as sea ice cover is low enough for sufficient light availability (Figure 9c).

3.4. Controls on Bloom Peak Biomass

According to model results at all 12 stations (Figures 9 and S3), light limitation is the dominant factor capping the maximum surface Chl a concentration, defined as the "bloom peak" (Figures 9a and S3a), in the ASP. In the polynya (excluding the marginal ice zone), surface Chl a concentrations are maximal when the combined light and iron availability (equation (21)) averages $3\% \pm 2\%$ of replete levels (Figures 9c and S3c, purple lines). When this level of limitation occurs, average mixed layer dFe concentration is $28\% \pm 5\%$ of replete concentration (Figure 9c, orange lines), while average mixed layer light is only $16\% \pm 9\%$ of the saturating level (Figure 9c, green lines).

The modeled bloom reaches its maximum Chl a concentration more quickly when mixed layers are shallower. At the five more stratified stations (Stations 6, 18, 25, 34, and 66), where the time-averaged mixed layer depth is <30 m between the bloom's start and peak, the bloom peak is reached 27 ± 5 days after the bloom starts. The bloom peak occurs much later than the maximum integrated GPP (13 ± 4 days after bloom start). At the other seven stations, where average prepeak mixed layer depths are >40 m, the bloom takes weeks longer to develop, with a 42 ± 10 day period between the beginning of the bloom and the peak of surface Chl a concentration. This lag between peak values of GPP and Chl a occurs because GPP in the model varies as the product of the nutrient uptake rate and phytoplankton biomass (section 2.8, equation (16)). In the model simulation, there is a little phytoplankton biomass at the beginning of the bloom, but very fast uptake rates result in high GPP before the onset of self-shading (Figures 9b and 9c). With fast rates of GPP, Chl a rapidly increases. However, even when GPP drops with the onset of light limitation, Chl a remains relatively steady since phytoplankton growth rates still exceed phytoplankton loss rates.

Maximum modeled seasonal Chl a concentrations precede minimum nutrient concentrations (Figures 9a, 9c, and S3a and S3c in the supporting information). After the peak in surface Chl a, phytoplankton continue to draw down nutrients, with maximum drawdown of surface concentrations of DIN and dFe occurring 15 ± 11 and 29 ± 10 days, respectively, after peak Chl a concentrations. Seasonal surface nutrient concentrations drop to values as low as 13 ± 1 mmol N/m^3 and 0.013 ± 0.007 μmol dFe/m^3 ($5 \pm 3\%$ replete). Over the period between the maximum Chl a concentration and the maximum dFe drawdown across all stations, surface Chl a concentrations decrease by 6 ± 2 mg/m^3 ($27\% \pm 7\%$).

3.5. Controls on Bloom Decline and Termination

When the combined effects of light and iron limitation cause phytoplankton losses to outweigh phytoplankton growth, the modeled bloom goes into decline. At the time of maximum dFe drawdown within the polynya (27 January 2011 $\pm$ 4 days), light and iron total availability is $0.9\% \pm 0.3\%$ (average across stations; Figures 9c and S3c), and Chl a concentrations drop precipitously. When the bloom goes into decline phytoplankton in the upper 100 m are lost mainly to aggregation ($63\% \pm 5\%$) and mortality ($28\% \pm 1\%$), while grazing ($7\% \pm 5\%$) and sinking ($2\% \pm 0.4\%$) are smaller loss terms (Figures 10 and S3e).

When the modeled bloom goes into decline, iron is more limiting than light, though light limitation by self-shading is still intense outside of the marginal ice zone. Within the polynya, light is $21\% \pm 5\%$ saturating and dFe is $8\% \pm 3\%$ replete when Chl a concentrations drop (Figure 9c). At the marginal ice zone, dFe is more limiting than light over the mixed layer (13% replete dFe versus 41% saturating light).
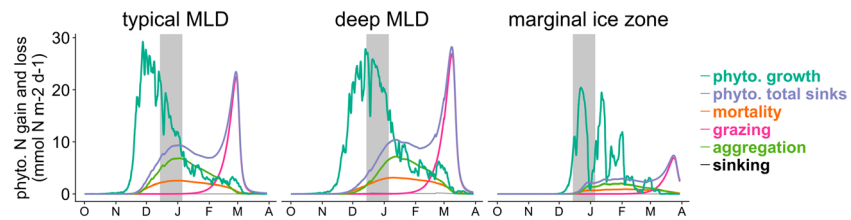
Figure 10. Time series of phytoplankton growth and losses at the same stations as in Figure 9, integrated over the top 100 m. The vertical gray bars show that the period Amundsen Sea Polynya International Research Expedition (ASPIRE) data are available. MLD = mixed layer depth.

Modeled grazing becomes significant only very late in the season, which may be an artifact of the grazing parameters being poorly constrained. According to model results, grazing did not become a significant sink for phytoplankton until after the ASPIRE sampling period. This result is consistent with ASPIRE observations (Wilson et al., 2015; Yager et al., 2016). Varying the zooplankton parameters, therefore, has little influence on the model-data fit during the beginning and height of the bloom. With the zooplankton parameter values that result in the bloom ending date closest to satellite observations (Arrigo et al., 2012), the maximum grazing rates integrated over the upper 100 m of the water column occur on 5 March 2011 (± 9 days), making up 95% $\pm$ 5% of the phytoplankton sinks on that date (Figures 10 and S3e).

3.6. Controls on Iron Cycling

All iron in the model is initially present in the dissolved phase and is transferred to the phytoplankton Fe pool. Dissolved Fe is taken up rapidly when early bloom primary productivity is high (Figures 11a and S3f). The dFe uptake rates decrease sharply and do not recover, however, with the early season decrease in primary production and rapid increase in light limitation (see section 3.3). While rates of dFe uptake by phytoplankton rise quickly with the initial development of the bloom, iron remineralization and scavenging rates increase more slowly, vertical (upper 100 m) integrals of remineralization and scavenging rates being highest, respectively, on 3 March 2011 (± 9 days) and on 2 February 2011 (± 27 days). By the bloom's peak, 46% $\pm$ 7% of iron present in the top 100 m is in the phytoplankton Fe pool, 15% $\pm$ 7% in small detritus, and 3% $\pm$ 1% in large detritus.

As the bloom goes into decline and ends, dFe uptake in surface waters at all stations drops and approaches zero, while iron remineralization, scavenging, and sinking decline more slowly and continue through the end of the modeled period (Figures 11b and S3g). As the bloom comes to an end, the dFe pool begins to increase again while the other three iron pools decline, with the phytoplankton Fe pool decreasing faster
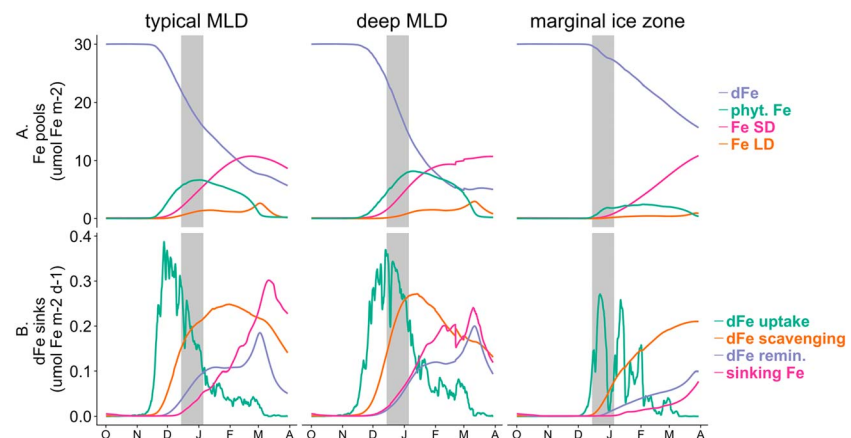

Figure 11. Time series of (a) Fe concentration in different pools integrated over the top 100 m, and (b) dFe fluxes integrated over the top 100 m at the same stations as shown in Figure 9. The vertical gray bars show that the period Amundsen Sea Polynya International Research Expedition (ASPIRE) data are available. MLD = mixed layer depth.

Table 3
Percentage Change in Total Seasonal Vertical Carbon Flux Below 100 m Following a 25% Increase in Biogeochemical Parameters

Parameter	Percent change in total seasonal vertical carbon flux
Maximum growth rate (P_{max})	+18
Sinking rate of large detritus (w_{LD})	+13
Initial slope of photosynthesis-irradiance curve (α)	+12
Aggregation rate of phytoplankton and small detritus (A)	+3
Maximum grazing rate (G_{max})	+3
Sinking rate of small detritus (w_{SD})	+3
Sinking rate of phytoplankton (w_P)	1
Remineralization rate of nitrogen in small detritus (R_{SD})	+<1
Nitrate uptake half-saturation constant (k_N)	0
Grazing half-saturation constant (k_P)	−2
Scavenging rate of dissolved Fe by small detritus (S_{SD})	−5
Mortality rate of phytoplankton (m_P)	−5
Excretion of nitrogen by zooplankton (E)	−6
Fe:N ratio for phytoplankton uptake (FeN)	−9
Remineralization rate of nitrogen in large detritus (R_{LD})	−9
Iron uptake half-saturation constant (k_F)	−17
Mortality of zooplankton (m_Z)	−23

than the detrital Fe pool. By the end of the modeled period on 31 March 2011, 39% ± 7% of iron is in the dissolved phase, 55% ± 10% in small detritus, 3% ± 2% in phytoplankton, and 3% ± 2% in large detritus.

3.7. Controls on Vertical Carbon Flux

Total seasonal vertical carbon flux across all stations is most sensitive to the phytoplankton growth parameters, the iron half-saturation constant, the zooplankton mortality rate, and the large detritus sinking rate (Table 3). Though zooplankton mortality does not strongly influence the cost function and therefore can hardly be constrained from the data considered for the assimilation, it has the largest impact on total seasonal vertical carbon flux across all stations among all the model's parameters. This impact occurs late in the season (Figure 10).

With the optimized values of the model parameters, vertical carbon flux at 100 m is highest after the ASPIRE sampling period, peaking at 3 March 2011 (±6 days), and is sustained to the end of the modeled period. Maximum vertical carbon flux at 100 m is generally higher at stations where MLDs are deeper (Figures 12 and S3h in the supporting information).

Large detrital particles compose 93% ± 4% of the vertical carbon flux at 100 m throughout the bloom across all stations. Since grazing is negligible in the first half of the bloom, (Figure 10 and S3e in the supporting information), the zooplankton contribution to the large particles is necessarily small (Figure 2), and the 100-m vertical carbon flux is largely driven by aggregated phytoplankton and small detritus. The peak in grazing rates corresponds to late-season peaks in vertical carbon flux at 100 m, indicating a late-season contribution by detritus from zooplankton grazing to the large detrital pool and to 100-m vertical carbon flux.

3.8. Low Winter dFe Scenario

When we run the model with the "no meltwater pump" scenario (a winter dFe concentration lowered to 0.1 μmol/m^3), the bloom reaches maximum Chl *a* concentrations less than half of those with a starting dFe concentration of 0.3 μmol/m^3 (Figure 13a versus Figure 9a). With this low winter dFe concentration, surface Chl *a* is lower, self-shading is lower, and therefore light limitation is weaker than iron limitation during the growth phase of the bloom (Figure 13b). Under these strongly iron-limited conditions, 100-m vertical carbon flux is a small fraction of that under higher dFe concentrations (Figure 13c versus Figure 12). Vertical carbon flux in this scenario is highest at the last time step of the modeled period, suggesting that the peak flux would occur sometime beyond the last date modeled. In this 1-D modeling exercise, the presence or absence of the meltwater pump is simulated only by changing the initial winter dFe concentration. In reality, the meltwater pump may bring additional dFe to the polynya euphotic zone through lateral advection and vertical mixing over the course of the bloom (St-Laurent et al., 2017), supplementing the
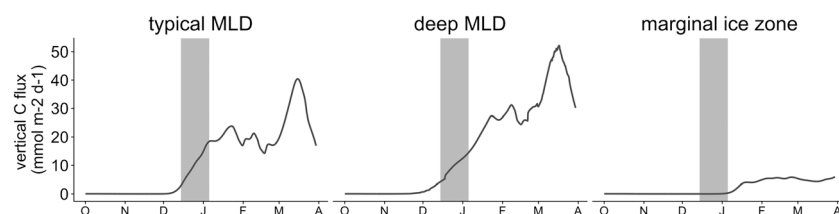

Figure 12. Time series of vertical carbon flux at 100 m at the same stations as in Figure 9. The vertical gray bars show that the period Amundsen Sea Polynya International Research Expedition (ASPIRE) data are available. MLD = mixed layer depth.

Figure 13. Time series for the model simulation with the low winter dFe concentration: (a) surface Chl *a* concentration, (b) light, iron, and combined light and iron availability (see equations (17), (19), and (21) in section 2.8) in the mixed layer, and (c) vertical carbon flux at 100 m at the same stations as in Figure 9. The green shaded regions in each panel in (b) show the light saturation at the 10% and 90% daily light levels. Note that the vertical scales in Figures 9a and 12 differ from those in panels (a) and (c) of this figure. The vertical gray bars show that the period Amundsen Sea Polynya International Research Expedition (ASPIRE) data are available. MLD = mixed layer depth.
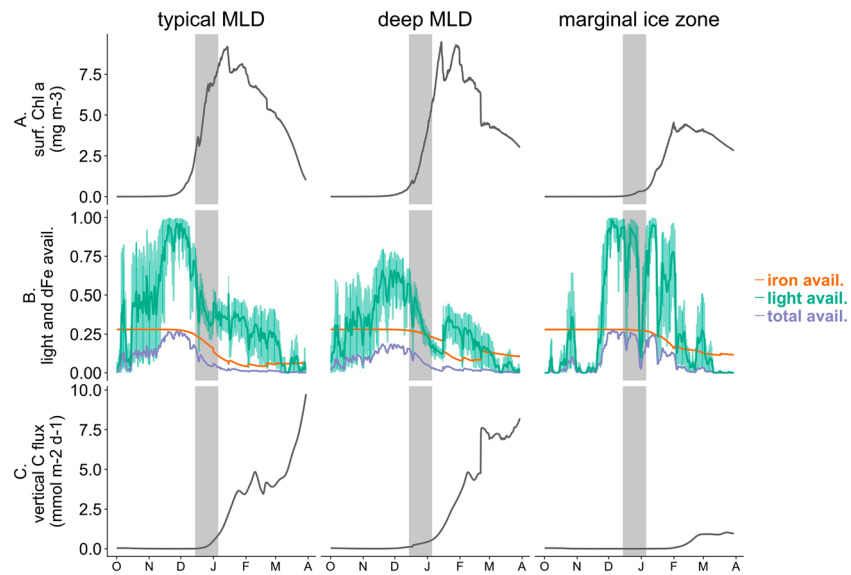
dFe available from the winter inventory. This effect can be simulated with a 3-D physical-biogeochemical model (St-Laurent et al., 2019).

4. Discussion

4.1. How Well Does a Relatively Simple 1-D Model Capture the Bloom Observed During ASPIRE?

For this study of the ASP, we examine controlling factors on the intense summer bloom with a 1-D idealized iron and nitrogen model for the top 210 m of the water column. Given the large set of poorly constrained model parameters, we use data assimilation to optimize the model, an approach shown to be useful for constraining biogeochemical parameters from a given set of observations (Friedrichs et al., 2007; Kaufman et al., 2018; Xiao & Friedrichs, 2014). By assimilating ASPIRE observations in a 1-D model, we are able to optimize efficiently the parameter values and test the model's parameter sensitivities. Despite the complexity of iron dynamics (Sherrell et al., 2015; Tagliabue et al., 2017) and the importance of horizontal advection of dFe into the ASP (St-Laurent et al., 2017), it is still possible for this relatively simple 1-D model to reproduce the substantial DIN drawdown and high Chl *a* concentrations observed during ASPIRE.

Our relatively simple model broadly explains the ASPIRE observations. The model accounts for most of the variability in observed concentrations of DIN ($r^2 = 0.80$, $p < 0.001$, when using all the ASPIRE data for the upper 200 m (87 degrees of freedom)), PON ($r^2 = 0.75$, $p < 0.001$, 67 degrees of freedom), and Chl *a* ($r^2 = 0.59$, $p < 0.001$, 68 degrees of freedom). The model-data fit for Chl *a* would likely be improved by using varying C: Chl *a* ratios, since a wide range of C:Chl *a* ratios were observed at the 12 stations during ASPIRE (47 ± 8 w/w, Yager et al., 2016) and *P. antarctica* can photoacclimate (Kropuenske et al., 2010), although this ability can be sensitive to iron concentrations (Van Leeuwe & Stefels, 2007). The variability in dFe is less well accounted for by the model ($r^2 = 0.19$, $p < 0.001$, for all 12 stations: 70 degrees of freedom), so model skill for dFe is lower than for DIN and Chl *a*. Because our model suggests that light is a more significant controlling factor than iron availability for the bloom during the ASPIRE sampling period, it is possible that discrepancies between the modeled and observed dFe profiles do not have a large impact on the ability of the model to simulate macronutrient cycling. Our analysis of the parameter sensitivity of the model-data fit supports the hypothesis that parameters critical to Fe cycling make little difference to the model-fit when dFe is available at relatively high concentrations. Our sensitivity analysis shows that the model-data fit is

more sensitive to phytoplankton growth and mortality parameters than to remineralization or scavenging parameters, which are important to Fe cycling in the model (Figure 4). Under conditions with low winter dFe, like our "no meltwater-pump" scenario, however, iron becomes the major controlling factor of the bloom (Figure 13). In Southern Ocean regions where dFe concentrations may be lower, more accurately reproducing the dissolved iron profiles may become important for explaining macronutrient cycling. There are also a number of other complex multivariate cost function possibilities (e.g., Wunsch, 2006) that may also improve the fit.

Although our treatments of iron and nitrogen cycling are necessarily different (Figure 2), modeled dFe profiles covary with modeled DIN profiles, unlike observed profiles of dFe and DIN (Figure 7). The covariation of dFe and DIN profiles in the model could be a result of poorly represented or missing processes, such as differential uptake or remineralization of N and Fe, and missing lateral inputs of Fe.

With a more complete description of remineralization and scavenging processes, profiles of dFe might be more accurately reproduced by the model. We assume that the rates of iron and nitrogen remineralization are equivalent and are independent of depth (Table 1), given a lack of relevant data for the ASP. By incorporating remineralization rates that are different for different nutrients and that vary with depth, the dFe profiles might be better captured (Boyd et al., 2017; Marchal & Lam, 2012). In addition, while the scavenging rate in our model is a function of the small particle concentration as well as the dFe concentration (second-order scavenging; Tagliabue et al., 2016), our model does not include complexation of dFe by organic iron-binding ligands. In reality, the presence of organic ligands may stabilize dFe at relatively high concentrations, such as observed at some stations in the ASP, even when Chl *a* is high and DIN is low (Figure 7). In other words, it is possible that ligand-bound dFe accumulated near the surface and was responsible for relatively high dFe observed when *P. antarctica* productivity was high. Determining the bioavailability of organically complexed iron (Hassler & Schoemann, 2009; Tagliabue et al., 2009) and vertical variations in ligand concentration would add additional complexity and perhaps lead to better model-data fit. More observations of the types and distribution of ligands in the ASP are necessary to appropriately model their effects on dFe distributions (Bundy et al., 2018; Hassler et al., 2017). Furthermore, our model does not explicitly include microbially mediated processes, which influence iron and cobalamin colimitation (Bertrand et al., 2015) nor does it include bacterial community structure, which may be important to the decline of the bloom (Delmont et al., 2014).

Horizontal advection of dFe in the ASP is likely important for the replenishment of dFe in the winter upper mixed layer (St-Laurent et al., 2017, 2019), but this initial winter concentration (chosen as 0.3 nM on 1 October 2010) is sufficient for the model to reach the high DIN drawdown and Chl *a* concentrations observed during ASPIRE. High concentrations of observed surface dFe at westernmost Stations 25 and 35 may be due to their proximity to the eastern sea ice edge of the polynya (Figures 1 and 7), where small amounts of dFe could be delivered by sea ice melt (St-Laurent et al., 2017), though $\delta^{18}O$ data do not indicate an unusually high sea ice contribution at these stations (Randall-Goodwin et al., 2015). Given the large supply of iron attributed to melting peripheral glaciers, it would be surprising for a 1-D model to estimate NCP accurately if the supply of iron depended entirely on lateral advection during the bloom season. Modeled NCP is indeed underestimated for the central and northern polynya, though modeled NCP is overestimated in the southern polynya near the ice shelves (Figure 8). This latitudinal relationship may be accounted for by the mixed layer depths. The southern stations where modeled NCP is overestimated (Stations 5, 13, and 57) are characterized by deeper mixed layers (Figure 3), which likely lead to higher integrated phytoplankton biomass than observed. In contrast, in the northern polynya, Stations 6, 34, and 66 are closer to the marginal ice zone and have shallower mixed layers (see Figure S3 in the supporting information), which result in smaller integrated phytoplankton biomass.

According to the model, peaks in vertical carbon flux at 100 m occur in March, whereas the peak in particle flux recorded from a moored sediment trap at 350 m near Station 57 occurred on 8 January (midpoint of a 1-week sampling interval), just 1 week after the surface Chl a peak, and was dominated by phytodetritus aggregates (Ducklow et al., 2015). Our model assumes sinking rates that do not account for the possibility of very rapid sinking of *P. antarctica* to depth (DiTullio et al., 2000); maxima of vertical particle fluxes simulated by the model are more related to zooplankton grazing than phytoplankton sinking. With faster sinking rates, it will take less time for aggregates of particles to sink to 100 m, so peaks in vertical carbon fluxes may

occur earlier. In the model, grazing appears to influence strongly both the magnitude and the timing of vertical carbon fluxes (Table 3 and Figures 10 and 12). In addition to the main flux maximum in March, the model generates additional smaller and broader carbon flux maxima in early January (Figure 12), more consistent with the timing of peaks apparent in the moored trap data. This discrepancy in the timing of carbon flux may arise because the parameters controlling zooplankton growth cannot be constrained by ASPIRE data and are chosen based on the bloom end date as determined by satellite data. The lack of zooplankton impact on the model-data fit is consistent with ASPIRE observations, which show a low abundance of zooplankton in the mixed layer, possibly resulting from the dominance of *P. antarctica*, which is generally unpalatable to grazers (Wilson et al., 2015). Given their apparent influence during the post-ASPIRE period according to the model, the grazing parameters need to be constrained better by additional observations.

4.2. What Is the Relative Importance of Light and Iron Availability?

Our model suggests that self-shading causes light to become limiting for the ASP phytoplankton bloom soon after its inception (Figure 9c), which is consistent with in situ observations (Park et al., 2017; Schofield et al., 2015). During the development of the bloom, modeled dFe is drawn down to 5% ± 3% of replete concentrations (relative to the iron half-saturation concentration of 0.26 μmol/m^3), which is consistent with the iron stress observed by Alderkamp et al. (2015). According to the model, at some stations, iron becomes more limiting than light later in the season, but it is the combination of intense self-shading paired with low dFe concentrations that causes the model bloom to decline. The decline of the bloom in the model occurs when the combined effects of aggregation, mortality, sinking, and grazing outweigh the growth of phytoplankton. In the model, phytoplankton losses exceed phytoplankton growth rates when growth rates sharply decline, while phytoplankton losses increase more gradually (Figure 10). Light availability can never completely suppress growth rates as long as there is some mixing of phytoplankton to the surface, so without strong iron limitation suppressing growth rates, the losses of phytoplankton may take longer to exceed phytoplankton growth and drive the decline of the bloom.

Since ASPIRE observed colonial *P. antarctica* experiencing significant light limitation through self-shading, we use a relatively high dFe half-saturation constant (lower affinity for iron) determined experimentally under similar conditions (Garcia et al., 2009). A transition from colonial *P. antarctica* to another phytoplankton group (such as diatoms or solitary *P. antarctica*) after the ASPIRE cruise left in January 2011, however, could result in significantly lower dFe half-saturation constants (with higher affinity for iron). Such a shift could further intensify iron limitation late in the season. While iron limitation is already strong under typical MLDs by the end of ASPIRE (Figure 9c), it is less limiting when MLDs are deeper. A lower iron half-saturation concentration (higher affinity) could reduce dFe faster at these stations with deeper MLDs, more closely resembling the iron limitation seen at stations with shallower MLDs.

It is important to note that our assessment of light and iron limitation in the ASP is reliant on fixed photo-physiological parameters. These parameters can be highly variable in the ocean. Nevertheless, the values assumed in our model strongly influence the model fit to the data (Figure 4), suggesting a high degree of phytoplankton physiological control relative to other biogeochemical processes. In addition, the photosynthesis-irradiance parameters may be affected by the degree of iron availability. Given iron's importance to the efficiency of Photosystem II (Raven, 1990), the photosynthesis-irradiance parameters $P_{\max}$ and α both increased with iron addition (Alderkamp et al., 2015). The photosynthesis-irradiance curve initial slope α is particularly important under low irradiance. Any shifts in α with changing Fe concentrations could significantly impact the bloom's progression after the onset of heavy light limitation.

Phytoplankton Fe:C ratios are also affected by both light limitation (Hopkinson et al., 2013; Sunda et al., 2014) and iron limitation (Strzepek et al., 2011, 2012). While cellular iron quotas may decrease under iron limitation, they may increase under light limitation, neither of which dependence is captured by the model. Our model shows very strong light limitation during the rise of the bloom, but physiological response to light limitation is dependent on the rate at which phytoplankton cells can photo-acclimate while being mixed in and out of the shallow euphotic zone (Schofield et al., 2015). The initial dFe concentration of 0.3 nM could therefore trigger either high Fe:C ratios (due to the relative abundance of dFe) or low Fe:C ratios (due to relatively abundant light at the beginning of the bloom). Our choice of a fixed Fe:C ratio may result in the

model either overestimating or underestimating dFe drawdown, and hence iron limitation later in the season. Observations of these processes may improve the model.

The importance of iron to the bloom would likely be diminished if applying a model that could better reproduce observations of dFe from ASPIRE. When advective processes are modeled (St-Laurent et al., 2019), dFe profiles are better captured, and for the entire season iron never becomes more limiting than the daily average light (see their Figure 9). In addition, surface concentrations of dFe from the model presented in this study are underestimated at most stations, suggesting that iron limitation may be weaker in a model that could better resolve the observed profiles. It is possible that higher dFe availability could delay the timing of the decline of the bloom, when modeled phytoplankton sinks outweigh growth.

4.3. How Can This Model be Applied to Other Polynyas, Other Phytoplankton Species, and Future Climate Scenarios?

The ASP is extraordinary among all Antarctic polynyas for its exceptionally intense productivity, likely due to the high basal melt rates of the nearby Dotson, Crosson, and Thwaites ice shelves. The meltwater pump mechanism driven by basal melting appears to be critical to relatively replete Winter Water reserves of iron (St-Laurent et al., 2019), which this study shows is critical to generate a bloom as intense as seen in the ASP (section 3.8). The *P. antarctica* bloom progression modeled here may be similar to those in other Antarctic coastal polynyas characterized by fairly deep MLDs and high basal melt rates of nearby ice shelves. Our model likely best represents the seasonal progression of iron-sensitive blooms where basal melt rates are higher and have the potential to create higher winter dFe concentrations. It may be less applicable to regions where mixed layers are shallower, such as stratified parts of the Ross Sea where diatoms dominate (Arrigo et al., 1999). The mixed layer depths of most of the 46 Antarctic polynyas are not yet known, however (Arrigo et al., 2015), so the relevance of this model to other Antarctic polynyas based on mixed layer depth is unknown. The model results presented may be increasingly relevant to polynyas experiencing decreasing sea ice duration (Stammerjohn et al., 2012) and therefore increased vertical mixing by winds.

Since the model used in this study is tuned particularly to *P. antarctica*, we would expect the model to produce considerably different results for Southern Ocean diatom species when considering their different uptake kinetics. While large ranges of possible k_F values have been reported for both *P. antarctica* and Southern Ocean diatoms (Coale et al., 2003; Timmermans et al., 2001, 2004), Fe:C ratios for diatoms under Fe-limited conditions have been found to be substationally lower than for *P. antarctica* (Strzepek et al., 2011). These lower Fe:C ratios would likely cause modeled drawdown of dFe by diatoms to be slower than for *P. antarctica*. In the Ross Sea, reported photosynthesis-irradiance parameters P_{max} and α are higher for *P. antarctica* than diatoms, and growth rates several times higher for *P. antarctica* than diatoms when light is available (Arrigo et al., 2010). If we were to apply these photosynthetic parameters to the model presented, we would anticipate much slower Fe uptake rates, and potentially much slower onset of light limitation imposed by phytoplankton self-shading.

Our model results demonstrate the importance of light to primary productivity in the ASP. Under climate change, the light regime will be affected by the decline of sea ice duration, as well as any changes in cloudiness. The spring retreat of sea ice in the Amundsen Sea is occuring increasingly early (Stammerjohn et al., 2015), which may in turn allow phytoplankton to bloom and become self-shading earlier. It is not known, however, how these effects could affect the seasonal primary productivity of the ASP, or the ability of the ASP to take up CO_2. More modeling is necessary to estimate how productivity in the ASP will change under continued warming, for which this study lays the groundwork.

5. Conclusion

In this study, we embed a relatively simple biogeochemical model modified from an existing iron model (Fiechter et al., 2009) in the vertical mixing model of ROMS to simulate the evolution of the bloom in the ASP. Although the iron model is a greatly simplified representation of iron cycling in the polynya, and although horizontal transport is neglected, we can explain much of the high Chl *a* concentrations observed in the ASP during the 2010–2011 austral summer. Most of the variability in DIN, Chl *a*, and PON is captured by the model (r^2 values of 0.80, 0.58, and 0.75, respectively), but observed profiles of dFe are less accurately

simulated ($r^2 = 0.19$). It is possible that more detailed parameterization of remineralization, scavenging, bioavailabilty, and dFe uptake could improve the simulation of dFe distributions.

Our sensitivity analysis shows that the model-data fit is more sensitive to phytoplankton growth and mortality parameters than to other biogeochemical parameters. In particular, when phytoplankton mortality rates are low, the fit becomes less sensitive to the remineralization, aggregation, and iron scavenging parameters. This result suggests a high degree of control by phytoplankton physiology on the bloom's development, relative to these other biogeochemical processes.

Our study suggests that the 2010–2011 ASP phytoplankton bloom was limited by light caused by self-shading for most of its duration but became increasingly limited by both light and iron as the bloom proceeded. The model results suggest that the bloom's decline is caused by strong limitation by light and iron, with zooplankton grazing only becoming important well after the initial decline in phytoplankton biomass. We also demonstrate that the depth of the mixed layer influences the development of the bloom. At stations where mixed layers are deep and the upper water column less stratified, iron limitation occurs later in the year, so the bloom peaks later. Deeper mixed layers also result in higher modeled vertical carbon fluxes. Vertical carbon flux in the model, however, is highly responsive to grazing parameters, which are poorly constrained by ASPIRE observations. The results from this research illustrate how light and Fe can both be important limiting factors in the development of the bloom in the ASP, which nevertheless achieves the highest primary productivity of any region on the Antarctic shelf.

References

Alderkamp, A.-C., van Dijken, G. L., Lowry, K. E., Connelly, T. L., Lagerström, M., Sherrell, R. M., et al. (2015). Fe availability drives phytoplankton photosynthesis rates during spring bloom in the Amundsen Sea Polynya, Antarctica. *Elementa: Science of the Anthropocene*, *3*(C), 000043. https://doi.org/10.12952/journal.elementa.000043

Arrigo, K. R., Lowry, K. E., & van Dijken, G. L. (2012). Annual changes in sea ice and phytoplankton in polynyas of the Amundsen Sea, Antarctica. *Deep-Sea Research Part II: Topical Studies in Oceanography*, 71-76, 5–15. https://doi.org/10.1016/j.dsr2.2012.03.006

Arrigo, K. R., Mills, M. M., Kropuenske, L. R., Van Dijken, G. L., Alderkamp, A. C., & Robinson, D. H. (2010). Photophysiology in two major southern ocean phytoplankton taxa: Photosynthesis and growth of *Phaeocystis antarctica* and fragilariopsis cylindrus under different irradiance levels. *Integrative and Comparative Biology*, *50*(6), 950–966. https://doi.org/10.1093/icb/icq021

Arrigo, K. R., Robinson, D. H., Worthen, D. L., Dunbar, R. B., DiTullio, G. R., VanWoert, M., & Lizotte, M. P. (1999). Phytoplankton community structure and the drawdown of nutrients and CO_2 in the Southern Ocean. *Science*, *283*(5400), 365–367. https://doi.org/10.1126/science.283.5400.365

Arrigo, K. R., & Van Dijken, G. L. (2003). Phytoplankton dynamics within 37 Antarctic coastal polynya systems. *Journal of Geophysical Research*, *108*(C8), 3271. https://doi.org/10.1029/2002JC001739

Arrigo, K. R., van Dijken, G. L., & Bushinsky, S. (2008). Primary production in the Southern. *Journal of Geophysical Research*, *113*, C08004. https://doi.org/10.1029/2007JC004551

Arrigo, K. R., Van Dijken, G. L., & Strong, A. L. (2015). Environmental controls of marine productivity hot spots around Antarctica. *Journal of Geophysical Research: Oceans*, *120*, 5545–5565. https://doi.org/10.1002/2015JC010888

Aumont, O., Ethé, C., Tagliabue, A., Bopp, L., & Gehlen, M. (2015). PISCES-v2: An ocean biogeochemical model for carbon and ecosystem studies. *Geoscientific Model Development*, *8*(8), 2465–2513. https://doi.org/10.5194/gmd-8-2465-2015

Becquevort, S., & Smith, W. O. (2001). Aggregation, sedimentation and biodegradability of phytoplankton-derived material during spring in the Ross Sea, Antarctica. *Deep-Sea Research Part II: Topical Studies in Oceanography*, *48*(19–20), 4155–4178. https://doi.org/10.1016/S0967-0645(01)00084-4

Bertrand, E. M., McCrow, J. P., Moustafa, A., Zheng, H., McQuaid, J. B., Delmont, T. O., et al. (2015). Phytoplankton–bacterial interactions mediate micronutrient colimitation at the coastal Antarctic sea ice edge. *Proceedings of the National Academy of Sciences*, *112*(32), 9938–9943. https://doi.org/10.1073/pnas.1501615112

Boyd, P. W., Ellwood, M. J., Tagliabue, A., & Twining, B. S. (2017). Biotic and abiotic retention, recycling and remineralization of metals in the ocean. *Nature Geoscience*. Nature Publishing Group, *10*(3), 167–173. https://doi.org/10.1038/ngeo2876

Bundy, R. M., Boiteau, R. M., McLean, C., Turk-Kubo, K. A., Mcilvin, M. R., Saito, M. A., et al. (2018). Distinct Siderophores siderophores Contribute contribute to Iron iron Cycling cycling in the Mesopelagic mesopelagic at Station station ALOHA. *Frontiers in Marine Science*, *5*, 1–15. https://doi.org/10.3389/fmars.2018.00061

Carvalho, F., Kohut, J., Oliver, M. J., & Schofield, O. (2017). Defining the ecologically relevant mixed layer depth for Antarctica's Coastal Seas. *Geophysical Research Letters*, *44*, 338–345. https://doi.org/10.1002/2016GL071205

Cavalieri, D. J., Markus, T., & Comiso, J. C. (2014). *AMSR-E aqua daily l3 12.5 km brightness temperature, sea ice concentration, and snow depth polar grids, version 3*. Boulder, Colo.: NASA National Snow and Ice Data Center Distributed Active Archive Center. https://doi.org/10.5067/AQUA/MODIS_OC.2014.0

Coale, K. H., Wang, X., Tanner, S. J., & Johnson, K. S. (2003). Phytoplankton growth and biological response to iron and zinc addition in the Ross Sea and Antarctic Circumpolar Current along 170°W. *Deep Sea Research Part II: Topical Studies in Oceanography*, *50*(3–4), 635–653. https://doi.org/10.1016/S0967-0645(02)00588-X

Dee, D. P., Uppala, S. M., Simmons, A. J., Berrisford, P., Poli, P., Kobayashi, S., et al. (2011). The ERA-Interim reanalysis: Configuration and performance of the data assimilation system. *Quarterly Journal of the Royal Meteorological Society*, *137*(656), 553–597. https://doi.org/10.1002/qj.828

Delmont, T. O., Hammar, K. M., Ducklow, H. W., Yager, P. L., & Post, A. F. (2014). *Phaeocystis antarctica* blooms strongly influence bacterial community structures in the Amundsen Sea polynya. *Frontiers in Microbiology*, *5*(DEC), 1–13. https://doi.org/10.3389/fmicb.2014.00646

DiTullio, G. R., Grebmeier, J. M., Arrigo, K. R., Lizotte, M. P., Robinson, D. H., Leventer, A., et al. (2000). Rapid and early export of *Phaeocystis antarctica* blooms in the Ross Sea, Antarctica. *Nature*, *404*(6778), 595–598. https://doi.org/10.1038/35007061

Ducklow, H. W., Wilson, S. E., Post, A. F., Stammerjohn, S. E., Erickson, M., Lee, S., et al. (2015). Particle flux on the continental shelf in the Amundsen Sea Polynya and Western Antarctic Peninsula. *Elementa: Science of the Anthropocene*, *3*, 000046. https://doi.org/10.12952/journal.elementa.000046

Evans, G. T., & Parslow, J. S. (1985). A model of annual plankton cycles. *Deep Sea Research Part B. Oceanographic Literature Review*, *32*(9), 759. https://doi.org/10.1016/0198-0254(85)92902-4

Fairall, C. W., Bradley, E. F., Hare, J. E., Grachev, A. A., & Edson, J. B. (2003). Bulk parameterization of air-sea fluxes: Updates and verification for the COARE algorithm. *Journal of Climate*, *16*(4), 571–591. https://doi.org/10.1175/1520-0442(2003)016 < 0571: BPOASF>2.0.CO;2

Fasham, M. J. R., Ducklow, H. W., & McKelvie, S. M. (1990). A nitrogen-based model of plankton dynamics in the ocean mixed layer. *Journal of Marine Research*, *48*(3), 591–639. https://doi.org/10.1357/002224090784984678

Fennel, K., Wilkin, J., Levin, J., Moisan, J., O'Reilly, J., & Haidvogel, D. (2006). Nitrogen cycling in the Middle Atlantic Bight: Results from a three-dimensional model and implications for the North Atlantic nitrogen budget. *Global Biogeochemical Cycles*, *20*, GB3007. https://doi.org/10.1029/2005GB002456

Fiechter, J., Moore, A. M., Edwards, C. A., Bruland, K. W., Di Lorenzo, E., Lewis, C. V. W., et al. (2009). Modeling iron limitation of primary production in the coastal Gulf of Alaska. *Deep-Sea Research Part II: Topical Studies in Oceanography*, *56*(24), 2503–2519. https://doi.org/10.1016/j.dsr2.2009.02.010

Friedrichs, M. A. M., Dusenberry, J. A., Anderson, L. A., Armstrong, R. A., Chai, F., Christian, J. R., et al. (2007). Assessment of skill and portability in regional marine biogeochemical models: Role of multiple planktonic groups. *Journal of Geophysical Research*, *112*, C08001. https://doi.org/10.1029/2006JC003852

Garcia, N., Sedwick, P., & DiTullio, G. (2009). Influence of irradiance and iron on the growth of colonial Phaeocystis antarctica: Implications for seasonal bloom dynamics in the Ross Sea, Antarctica. *Aquatic Microbial Ecology*, *57*, 203–220. https://doi.org/10.3354/ame01334

Gerringa, L. J. A., Alderkamp, A.-C. C., Laan, P., Thuróczy, C.-E. E., de Baar, H. J. W., Mills, M. M., et al. (2012). Iron from melting glaciers fuels the phytoplankton blooms in Amundsen Sea (Southern Ocean): Iron biogeochemistry. *Deep Sea Research Part II: Topical Studies in Oceanography*, *71-76*, 16–31. https://doi.org/10.1016/j.dsr2.2012.03.007

Greisman, P. (1979). On upwelling driven by the melt of ice shelves and tidewater glaciers. *Deep Sea Research Part A: Oceanographic Research Papers*, *26*(9), 1051–1065. https://doi.org/10.1016/0198-0149(79)90047-5

Grieger, J., Leckebusch, G. C., & Ulbrich, U. (2016). Net precipitation of Antarctica: Thermodynamical and dynamical parts of the climate change signal. *Journal of Climate*, *29*(3), 907–924. https://doi.org/10.1175/JCLI-D-14-00787.1

Hahm, D., Rhee, T. S., Kim, H.-C., Park, J., Kim, Y., Shin, H. C., & Lee, S. (2014). Spatial and temporal variation of net community production and its regulating factors in the Amundsen Sea, Antarctica. *Journal of Geophysical Research: Oceans*, *119*, 2815–2826. https://doi.org/10.1002/2013JC009762

Hassler, C. S., & Schoemann, V. (2009). Bioavailability of organically bound Fe to model phytoplankton of the Southern Ocean. *Biogeosciences*, *6*(10), 2281–2296. https://doi.org/10.5194/bg-6-2281-2009

Hassler, C. S., van den Berg, C. M. G., & Boyd, P. W. (2017). Toward a regional classification to provide a more inclusive examination of the ocean biogeochemistry of iron-binding ligands. *Frontiers in Marine Science*, *4*. https://doi.org/10.3389/fmars.2017.00019

Hayes, C. T., Black, E. E., Anderson, R. F., Baskaran, M., Buesseler, K. O., Charette, M. A., et al. (2018). Flux of particulate elements in the North Atlantic Ocean constrained by multiple radionuclides. *Global Biogeochemical Cycles*, *32*(12), 1738–1758. https://doi.org/10.1029/2018GB005994

Hedström, K. S. (2009). Technical manual for a coupled sea-ice/ocean circulation model (version 3). *University of Alaska Fairbanks Arctic Region Supercomputing Center Tech. Rep. OCS Study MMS 2009-062*. Retrieved from https://www.myroms.org/wiki/images/3/3b/Manual22010.pdf

Helton, J. C., & Davis, F. J. (2003). Latin hypercube sampling and the propagation of uncertainty in analyses of complex systems. *Reliability Engineering and System Safety*, *81*(1), 23–69. https://doi.org/10.1016/S0951-8320(03)00058-9

Hopkinson, B. M., Seegers, B., Hatta, M., Measures, C. I., Greg Mitchell, B., & Barbeau, K. A. (2013). Planktonic C: Fe ratios and carrying capacity in the southern Drake Passage. *Deep-Sea Research Part II: Topical Studies in Oceanography*, *90*, 102–111. https://doi.org/10.1016/j.dsr2.2012.09.001

Hyun, J.-H., Kim, S.-H., Yang, E. J., Choi, A., & Lee, S. H. (2016). Biomass, production, and control of heterotrophic bacterioplankton during a late phytoplankton bloom in the Amundsen Sea Polynya, Antarctica. *Deep Sea Research Part II: Topical Studies in Oceanography*, *123*, 102–112. https://doi.org/10.1016/j.dsr2.2015.10.001

Kaufman, D. E., Friedrichs, M. A. M., Hemmings, J. C. P., & Smith, W. O. (2018). Assimilating bio-optical glider data during a phytoplankton bloom in the southern Ross Sea. *Biogeosciences*, *15*(1), 73–90. https://doi.org/10.5194/bg-15-73-2018

Kim, M., Hwang, J., Kim, H. J., Kim, D., Yang, E. J., Ducklow, H. W., et al. (2015). Sinking particle flux in the sea ice zone of the Amundsen Shelf, Antarctica. *Deep Sea Research, Part I*, *101*, 110–117. https://doi.org/10.1016/j.dsr.2015.04.002

Kim, M., Hwang, J., Lee, S. H., Kim, H. J., Kim, D., Yang, E. J., & Lee, S. (2016). Sedimentation of particulate organic carbon on the Amundsen Shelf, Antarctica. *Deep-Sea Research Part II*, *123*, 135–144. https://doi.org/10.1016/j.dsr2.2015.07.018

Kropuenske, L. R., Mills, M. M., Van Dijken, G. L., Alderkamp, A. C., Mine Berg, G., Robinson, D. H., et al. (2010). Strategies and rates of photoacclimation in two major southern ocean phytoplankton taxa: Phaeocystis Antarctica (haptophyta) and Fragilariopsis Cylindrus (bacillariophyceae). *Journal of Phycology*, *46*(6), 1138–1151. https://doi.org/10.1111/j.1529-8817.2010.00922.x

Kurtz, N. T., & Markus, T. (2012). Satellite observations of Antarctic sea ice thickness and volume. *Journal of Geophysical Research*, *117*, C08025. https://doi.org/10.1029/2012JC008141

Large, W. G., McWilliams, J. C., & Doney, S. C. (1994). Oceanic vertical mixing: A review and a model with a nonlocal boundary layer parameterization. *Reviews of Geophysics*, *32*(4), 363. https://doi.org/10.1029/94RG01872

Lee, S. H., Hwang, J., Ducklow, H. W., Hahm, D., Lee, S. H., Kim, D., et al. (2017). Evidence of minimal carbon sequestration in the productive Amundsen Sea polynya. *Geophysical Research Letters*, *44*, 7892–7899. https://doi.org/10.1002/2017GL074646

Lee, S. H., Kim, B. K., Yun, M. S., Joo, H., Yang, E. J., Kim, Y. N., et al. (2012). Spatial distribution of phytoplankton productivity in the Amundsen Sea, Antarctica. *Polar Biology*, *35*(11), 1721–1733. https://doi.org/10.1007/s00300-012-1220-5

Lee, Y., Yang, E. J., Park, J., Jung, J., Kim, T. W., & Lee, S. H. (2016). Physical-biological coupling in the Amundsen Sea, Antarctica: Influence of physical factors on phytoplankton community structure and biomass. *Deep-Sea Research Part I: Oceanographic Research Papers*, *117*, 51–60. https://doi.org/10.1016/j.dsr.2016.10.001

Lee, Y. C., Park, M. O., Jung, J., Yang, E. J., & Lee, S. H. (2016). Taxonomic variability of phytoplankton and relationship with production of CDOM in the polynya of the Amundsen Sea, Antarctica. *Deep-Sea Research Part II: Topical Studies in Oceanography*, *123*, 30–41. https://doi.org/10.1016/j.dsr2.2015.09.002

Marchal, O., & Lam, P. J. (2012). What can paired measurements of Th isotope activity and particle concentration tell us about particle cycling in the ocean? *Geochimica et Cosmochimica Acta*, *90*, 126–148. https://doi.org/10.1016/j.gca.2012.05.009

Matsumoto, K., Tokos, K., Huston, A., & Joy-Warren, H. (2013). MESMO 2: A mechanistic marine silica cycle and coupling to a simple terrestrial scheme. *Geoscientific Model Development*, *6*(2), 477–494. https://doi.org/10.5194/gmd-6-477-2013

Mockus, J. (1989). *Bayesian Approach to Global Optimization*. (Vol. 123). Dordrecht, Netherlands: Springer. https://doi.org/10.1007/978-94-009-0909-0

Mu, L., Stammerjohn, S. E., Lowry, K. E., & Yager, P. L. (2014). Spatial variability of surface pCO_2 and air-sea CO_2 flux in the Amundsen Sea Polynya, Antarctica. *Elementa: Science of the Anthropocene*, *2*, 000036. https://doi.org/10.12952/journal.elementa.000036

Parekh, P., Follows, M. J., & Boyle, E. A. (2005). Decoupling of iron and phosphate in the global ocean. *Global Biogeochem Cycles*, *19*(2). https://doi.org/10.1029/2004GB002280

Park, J., Kuzminov, F. I., Bailleul, B., Yang, E. J., Lee, S. H., Falkowski, P. G., & Gorbunov, M. Y. (2017). Light availability rather than Fe controls the magnitude of massive phytoplankton bloom in the Amundsen Sea polynyas, Antarctica. *Limnology and Oceanography*, *62*(5), 2260–2276. https://doi.org/10.1002/lno.10565

Powers, J. G., Manning, K. W., Bromwich, D. H., Cassano, J. J., & Cayette, A. M. (2012). A decade of antarctic science support through AMPS. *Bulletin of the American Meteorological Society*, *93*(11), 1699–1712. https://doi.org/10.1175/BAMS-D-11-00186.1

Rafter, P. A., Sigman, D. M., & Mackey, K. R. M. (2017). Recycled iron fuels new production in the eastern equatorial Pacific Ocean. *Nature Communications*, *8*(1), 1100. https://doi.org/10.1038/s41467-017-01219-7

Randall-Goodwin, E., Meredith, M. P., Jenkins, A., Yager, P. L., Sherrell, R. M., Abrahamsen, E. P., et al. (2015). Freshwater distributions and water mass structure in the Amundsen Sea Polynya region, Antarctica. *Elementa: Science of the Anthropocene*, *3*, 000065. https://doi.org/10.12952/journal.elementa.000065

Raven, J. A. (1990). Predictions of Mn and Fe use efficiencies of phototrophic growth as a function of light availability for growth and of C assimilation pathway. *New Phytologist*, *116*(1), 1–18. https://doi.org/10.1111/j.1469-8137.1990.tb00505.x

Redfield, A. C. (1963). The influence of organisms on the composition of sea-water. In M. N. Hill (Ed.), *The Sea*, (Vol. II, pp. 26–77). New York: John Wiley.

Saito, M. A., Goepfert, T. J., & Ritt, J. T. (2008). Some thoughts on the concept of colimitation: Three definitions and the importance of bioavailability. *Limnology and Oceanography*, *53*(1), 276–290. https://doi.org/10.4319/lo.2008.53.1.0276

Schofield, O. M., Miles, T., Alderkamp, A.-C., Lee, S., Haskins, C., Rogalsky, E., et al. (2015). In situ phytoplankton distributions in the Amundsen Sea Polynya measured by autonomous gliders. *Elementa: Science of the Anthropocene*, *3*, 000073. https://doi.org/10.12952/journal.elementa.000073

Sedwick, P. N., Garcia, N. S., Riseman, S. F., Marsay, C. M., & DiTullio, G. R. (2007). Evidence for high iron requirements of colonial *Phaeocystis antarctica* at low irradiance. *Biogeochemistry*, *83*(1–3), 83–97. https://doi.org/10.1007/s10533-007-9081-7

Shchepetkin, A. F., & McWilliams, J. C. (2005). The regional oceanic modeling system (ROMS): A split-explicit, free-surface, topography-following-coordinate oceanic model. *Ocean Modelling*, *9*(4), 347–404. https://doi.org/10.1016/j.ocemod.2004.08.002

Sherrell, R. M., Lagerström, M. E., Forsch, K. O., Stammerjohn, S. E., & Yager, P. L. (2015). Dynamics of dissolved iron and other bioactive trace metals (Mn, Ni, Cu, Zn) in the Amundsen Sea Polynya, Antarctica. *Elementa: Science of the Anthropocene*, *3*, 000071. https://doi.org/10.12952/journal.elementa.000071

Snoek, J., Larochelle, H., & Adams, R. P. (2012). Practical Bayesian optimization of machine learning algorithms. *Advances in Neural Information Processing Systems*, *25*, 2951–2959.

Stammerjohn, S., Massom, R., Rind, D., & Martinson, D. (2012). Regions of rapid sea ice change: An inter-hemispheric seasonal comparison. *Geophysical Research Letters*, *39*, L06501. https://doi.org/10.1029/2012GL050874

Stammerjohn, S. E., Maksym, T., Massom, R. a., Lowry, K. E., Arrigo, K. R., Yuan, X., et al. (2015). Seasonal sea ice changes in the Amundsen Sea, Antarctica, over the period of 1979–2014. *Elementa: Science of the Anthropocene*, *3*(1), 000055. https://doi.org/10.12952/journal.elementa.000055

Stammerjohn, S. E., Martinson, D. G., Smith, R. C., & Iannuzzi, R. A. (2008). Sea ice in the western Antarctic Peninsula region: Spatio-temporal variability from ecological and climate change perspectives. *Deep-Sea Research Part II: Topical Studies in Oceanography*, *55*(18–19), 2041–2058. https://doi.org/10.1016/j.dsr2.2008.04.026

Stein, M. (2012). Large sample properties of simulations using Latin hypercube sampling. *Technometrics*, *29*(2), 143–141. https://doi.org/10.2307/1269769

St-Laurent, P., Yager, P. L., Sherrell, R. M., Oliver, H., Dinniman, M. S., & Stammerjohn, S. E. (2019). Modeling the seasonal cycle of iron and carbon fluxes in the Amundsen Sea Polynya, Antarctica. *Journal of Geophysical Research: Oceans*, *124*(3), 1544–1565. https://doi.org/10.1029/2018JC014773

St-Laurent, P., Yager, P. L., Sherrell, R. M., Stammerjohn, S. E., & Dinniman, M. S. (2017). Pathways and supply of dissolved iron in the Amundsen Sea (Antarctica). *Journal of Geophysical Research: Oceans*, *122*, 7135–7162. https://doi.org/10.1002/2017JC013162

Strzepek, R. F., Hunter, K. A., Frew, R. D., Harrison, P. J., & Boyd, P. W. (2012). Iron-light interactions differ in Southern Ocean phytoplankton. *Limnology and Oceanography*, *57*(4), 1182–1200. https://doi.org/10.4319/lo.2012.57.4.1182

Strzepek, R. F., Maldonado, M. T., Hunter, K. A., Frew, R. D., & Boyd, P. W. (2011). Adaptive strategies by Southern Ocean phytoplankton to lessen iron limitation: Uptake of organically complexed iron and reduced cellular iron requirements. *Limnology and Oceanography*, *56*(6), 1983–2002. https://doi.org/10.4319/lo.2011.56.6.1983

Sunda, W. G., Sunda, W. G., & Huntsman, S. A. (2014). Interrelated influence of iron, light and cell size on marine phytoplankton growth light and cell size on marine. *Nature*, *390*(6658), 389–392. https://doi.org/10.1038/37093

Tagliabue, A., Aumont, O., DeAth, R., Dunne, J. P., Dutkiewicz, S., Galbraith, E., et al. (2016). How well do global ocean biogeochemistry models simulate dissolved iron distributions? *Global Biogeochemical Cycles*, *30*, 149–174. https://doi.org/10.1002/2015GB005289

Tagliabue, A., Bopp, L., Aumont, O., & Arrigo, K. R. (2009). Influence of light and temperature on the marine iron cycle: From theoretical to global modeling. *Global Biogeochemical Cycles*, *23*, GB2017. https://doi.org/10.1029/2008GB003214

Tagliabue, A., Bowie, A. R., Boyd, P. W., Buck, K. N., Johnson, K. S., & Saito, M. A. (2017). The integral role of iron in ocean biogeochemistry. *Nature*. Nature Publishing Group, *543*(7643), 51–59. https://doi.org/10.1038/nature21058

Timmermans, K. R., Gerringa, L. J. A., de Baar, H. J. W., van der Wagt, B., Veldhuis, M. J. W., de Jong, J. T. M., et al. (2001). Growth rates of large and small Southern Ocean diatoms in relation to availability o iron in natural seawater. *Limnology and Oceanography*, *46*(2), 260–266. https://doi.org/10.4319/lo.2001.46.2.0260

Timmermans, K. R., Van Der Wagt, B., & De Baar, H. J. W. (2004). Growth rates, half-saturation constants, and silicate, nitrate, and phosphate depletion in relation to iron availability of four large, open-ocean diatoms from the Southern Ocean. *Limnology and Oceanography*, *49*(6), 2141–2151. https://doi.org/10.4319/lo.2004.49.6.2141

Van Leeuwe, M. A., & Stefels, J. (2007). Photosynthetic responses in *Phaeocystis antarctica* towards varying light and iron conditions. *Biogeochemistry*, *83*, 61–70. https://doi.org/10.1007/978-1-4020-6214-8_6

Wang, S., & Moore, J. K. (2011). Incorporating Phaeocystis into a Southern Ocean ecosystem model. *Journal of Geophysical Research*, *116*, C01019. https://doi.org/10.1029/2009JC005817

Wilson, S. E., Swalethorp, R., Kjellerup, S., Wolverton, M. A., Ducklow, H. W., & Yager, P. L. (2015). Meso- and macro-zooplankton community structure of the Amundsen Sea Polynya, Antarctica (Summer 2010–2011). *Elementa: Science of the Anthropocene*, *3*, 1–14. https://doi.org/10.12952/journal.elementa.000033

Wunsch, C. (2006). *Discrete Inverse and State Estimation Problems: With Geophysical Fluid Applications*, (p. 371). Cambridge: Cambridge Un. Press. https://doi.org/10.1017/CBO9780511535949

Xiao, Y., & Friedrichs, M. A. M. (2014). Using biogeochemical data assimilation to assess the relative skill of multiple ecosystem models in the Mid-Atlantic Bight: Effects of increasing the complexity of the planktonic food web. *Biogeosciences*, *11*(11), 3015–3030. https://doi.org/10.5194/bg-11-3015-2014

Xie, H., Tekeli, A. E., Ackley, S. F., Yi, D., & Zwally, H. J. (2013). Sea ice thickness estimations from ICESat Altimetry over the Bellingshausen and Amundsen Seas, 2003–2009. *Journal of Geophysical Research: Oceans*, *118*, 2438–2453. https://doi.org/10.1002/jgrc.20179

Yager, P. L., Sherrell, R. M., Stammerjohn, S. E., Alderkamp, A.-C., Schofield, O. M., Abrahamsen, E. P., et al. (2012). ASPIRE: The Amundsen Sea Polynya International Research Expedition. *Oceanography*, *25*(3), 40–53. https://doi.org/10.5670/oceanog.2012.73

Yager, P. L., Sherrell, R. M., Stammerjohn, S. E., Ducklow, H. W., Schofield, O. M. E., Ingall, E. D., et al. (2016). A carbon budget for the Amundsen Sea Polynya, Antarctica: Estimating net community production and export in a highly productive polar ecosystem. *Elementa: Science of the Anthropocene*, *4*, 000140. https://doi.org/10.12952/journal.elementa.000140

Yang, E. J., Jiang, Y., & Lee, S. H. (2016). Microzooplankton herbivory and community structure in the Amundsen Sea, Antarctica. *Deep Sea Research Part II: Topical Studies in Oceanography*, *123*, 58–68. https://doi.org/10.1016/j.dsr2.2015.06.001